Thermal Modeling of Directed Energy Deposition Additive Manufacturing using Graph Theory

Structured Abstract

Purpose of this paper

The objective of this work is to develop, apply, and validate a mesh-free graph theory-based approach for rapid thermal modeling of the directed energy deposition (DED) additive manufacturing process.

Design/methodology/approach

In the current work, we develop a novel mesh-free graph theory-based approach to predict the thermal history of the DED process. Subsequently, we validated the graph theory predicted temperature trends using experimental temperature data for DED of titanium alloy parts (Ti-6Al-4V). Temperature trends were tracked by embedding thermocouples in the substrate. The DED process was simulated using the graph theory approach, and the thermal history predictions were validated based on the data from the thermocouples.

Practical implications

The DED process is particularly valuable for near-net shape manufacturing, repair and remanufacturing applications. However, DED parts are often afflicted with flaws, such as cracking and distortion. In DED, flaw formation is largely governed by the intensity and spatial distribution of heat in the part during the process, often referred to as the thermal history. Accordingly, fast and accurate thermal models to predict the thermal history are necessary to understand and preclude flaw formation.

Findings

The temperature trends predicted by the graph theory approach have mean absolute percentage error of ~11% and root mean square error of 23 °C when compared to the experimental data. Moreover, the graph theory simulation was obtained within 4 minutes using desktop computing resources, which is less than the build time of 25 minutes. By comparison, a finite element-based model required 136 minutes to converge to similar level of error.

Research limitations/implications

We use data from fixed thermocouples when printing thin-wall DED parts. In the future we will incorporate infrared thermal camera data from large parts.

Originality/value

This paper presents a new mesh-free computational thermal modeling approach based on graph theory (network science) and applies it to DED. The approach eschews the tedious and computationally demanding aspect of finite element modeling and allows rapid simulation of the thermal history in additive manufacturing. While graph theory has been applied to thermal modeling of laser powder bed fusion (LPBF), there are distinct phenomenological differences between DED and LPBF that necessitate substantial modifications to the graph theory approach.

Keywords: Thermal Modeling, Directed Energy Deposition, Titanium Alloy, Graph Theory.

1 Introduction

1.1 Objective and Motivation

The objective of this work is to develop, apply, and validate a mesh-free graph theory-based approach for rapid prediction of the temperature distribution in parts made using the directed energy deposition (DED) additive manufacturing process. In the DED process, as exemplified in Figure 1, metal powder is sprayed onto a substrate and melted using energy from a laser. The relative motion of the laser and substrate results in a three-dimensional geometry [1]. The DED process is particularly valuable for rapid repair or upgrading of damaged or legacy components, enabling the affordable addition of complex features. The process can also enhance existing parts with protective wear or thermal barrier coatings [2, 3].

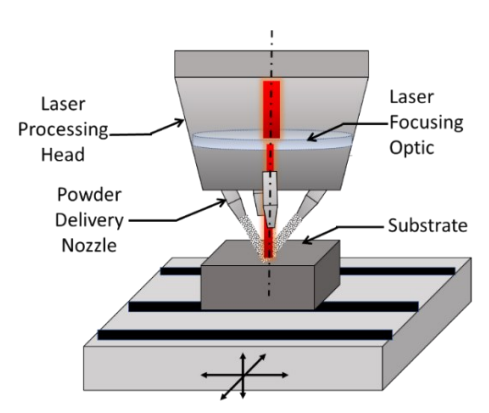


Figure 1: Schematic of the DED process. Metal powder is sprayed via nozzles and fused onto a substrate by a laser beam.

However, the DED process has a tendency to create flaws, such as cracks, distortion, and non-uniform (heterogeneous) microstructure [4, 5]. Despite significant advantages over conventional subtractive and formative manufacturing, safety-critical industries such as aerospace and defense are reticent in adopting the DED process due to the lack of consistent part properties. Consequently, there is an ongoing effort to understand the causal linkage between fundamental process phenomena, flaw formation, and physio-mechanical properties of the part in DED [4, 6].

In the DED process, the temperature distribution inside the part during deposition, typically called the *thermal history* or temperature field, influences flaw formation, such as microstructural heterogeneity, porosity, and deformation [7]. The temperature distribution is a function of the part geometry, process parameters, and material properties [8]. Accordingly, fast and accurate approaches to predict the thermal history in DED prior to printing the part are required for understanding and preventing flaw formation. In addition, these approaches should enable new critical functions including, but not limited to, predicting the final geometry of the part, process optimization and model-based process control, as depicted in Figure 2 [9, 10]. Hence, there is a strong need to approximate (simulate) the thermal history of DED parts before manufacturing is completed, beginning with the designed (ideal) geometry.

For example, the rapid prediction (simulation) of thermal history is valuable for identifying and remedying potential red-flag problems, such as overheating, before the part is printed. Consequently, different process tool path strategies, part orientation, and process parameter combinations can be tested and optimized *in silico* using thermal simulations. Thus, reducing the time and experimental effort required for process optimization.

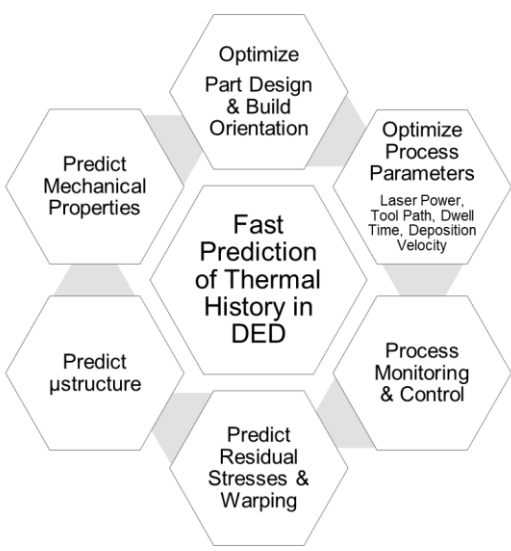


Figure 2: Fast and accurate modeling of the thermal history is central to quality assurance of DED.

1.2 Challenges and Novelty

Recent review articles emphasize the need for accurate and fast computational approaches to predict part thermal history in DED [7-9, 11, 12]. These review papers also summarize validation efforts by various researchers. The main challenge in part-scale thermal modeling of the DED process is that mesh-based finite element (FE) thermal models are relatively slow with computation time extending to hours if not days for a multi-layered practical part [13-15]. While commercial thermal simulation software for other additive manufacturing processes, such as laser powder bed fusion, have reduced the computation effort, development of such tools for DED is in their nascency. The novelty of this work is as follows:

- All current approaches for thermal modeling in DED use the finite element method. This research addresses the foregoing challenge by devising a mesh-free graph theory-based computational thermal modeling approach to predict the temperature distribution in DED parts. The graph theory approach has previously been published in the context of the laser powder bed fusion (LPBF) process [16-18]. The approach is verified to be five to ten times faster than finite element modeling, enabling the prediction of thermal history using desktop computing in the context of the LPBF process.
- This paper develops, applies, and validates the graph theory approach in the context of the
 DED process. As will be explained in Sec. 4, the considerable phenomenological differences
 between the LPBF and DED processes necessitates significant changes to the graph theory
 approach for application to the latter.

The rest of this paper is organized as follows. Sec. 2. summarizes the salient literature in thermal modeling in DED from the context of FE modeling. In Sec. 3, we detail the experimental methodology for the acquisition of temperature data during DED manufacturing of titanium alloy

thin wall parts. Next, in Sec. 4, the graph theory approach for thermal modeling in DED is described in depth. In Sec. 5 the temperature trends predicted using the graph theory approach are validated with experimental trends and compared to the FE-based predictions published in the literature [19, 20]. Conclusions and avenues for future work are delineated in Sec. 6.

2 Literature Review

Recent review articles emphasize the need for accurate and fast computational approaches to predict part thermal history in DED [7-9, 11, 12]. These review papers also summarize validation efforts by various researchers. Michaleris pioneered FE-based techniques for thermal modeling of AM processes, including DED [21]. Michaleris proposed and tested two material deposition methods [22]: (1) *quiet* element, and (2) *inactive* element. In the quiet element method, the entire part is meshed, but elements representing undeposited material are assigned infinitesimal thermal conductivity values. In the inactive element approach, the deposition process is mimicked by activating elements at each time step. The graph theory approach proposed in this work uses the inactive element technique to simulate the DED process.

Three major approximations for incorporating convective heat losses in DED have been studied [7-9, 11, 12]. First, as commonly implemented in FE-based modeling of the welding process, researchers have considered convective heat loss to be negligible in DED [23-27]. Second, heat loss through free convection is assumed to occur uniformly over all surfaces [28-34]. Third, accelerated heat loss due to forced convection is considered on all free surfaces as a result of the carrier gas flow [35, 36]. Notably, an effort to develop a measurement-based forced convection model was proposed and tested by Heigel *et al.* [19, 20]. Heigel and co-workers further compared their proposed model with other assumed convection regimes [37]. Heigel and co-workers

demonstrated that a forced convection model will produce more accurate simulation results than a model that considers only free convection or no convection at all.

Accordingly, in the present work, a combination of free and forced convection regimes are considered. As will be explained in Sec. 4.3, heat loss due to forced convection is assumed for all part surfaces over which there is a predominant flow of carrier gas. Heat loss due to free convection is assumed at surfaces that are not directly affected by the carrier gas, such as the bottom and sides of the substrate.

3 Methods

3.1 Experimental Builds

Data for this work was provided by Heigel *et al.* and is described in Ref. [19, 20]. Single-track thin walls were deposited with an Optomec MR-7 DED system. In a single-track thin wall part, material in a layer is deposited in a single pass, i.e., a layer has only one hatch. The material used is ASTM standard Ti-6Al-4V powder. Parts were manufactured on a 6.4 mm thick Ti-6Al-4V substrate clamped on one end according to the schematic in Figure 3. Argon shielding gas was used during the DED process at a rate of 30 L/min. The laser used in the process is a 500 W IPG Photonics fiber laser with a beam diameter of 1.5 mm. 62 layers were deposited with a nominal hatch thickness of 0.173mm.

Two thin-walled parts labeled as Case A and Case B (Figure 3), are studied in this work. The processing conditions for the two cases are summarized in Table 1. We have chosen to study these two parts as the process parameters are identical in all respects, except the dwell time between layers. The dwell time governs the cooling behavior in DED and has a consequential effect on the evolved microstructure and properties [38, 39].

The parts are designed to have dimensions 37.2 mm × 3 mm × ~11 mm (vertical height) and consist of 62 layers deposited onto a Ti-6Al-4V substrate with dimensions 76.2 mm × 25.4 mm × 6.4 mm (L×W×H) [19, 20]. Each thin wall is built on a separate substrate, which is clamped at one end. The deposition direction alternates for each layer; The laser travels in one direction for odd-numbered layers and the opposite direction for even-numbered layers. After a layer is completed, the laser is disabled to cease powder sintering. Powder flow does not stop during this period to ensure consistent deposition for subsequent layers. While the nominal laser power is set at 500 W, the actual power delivered using a power probe and ascertained the power to be between 410 W and 415 W [19, 20]. The process parameter distinctions between the cases are as follows.

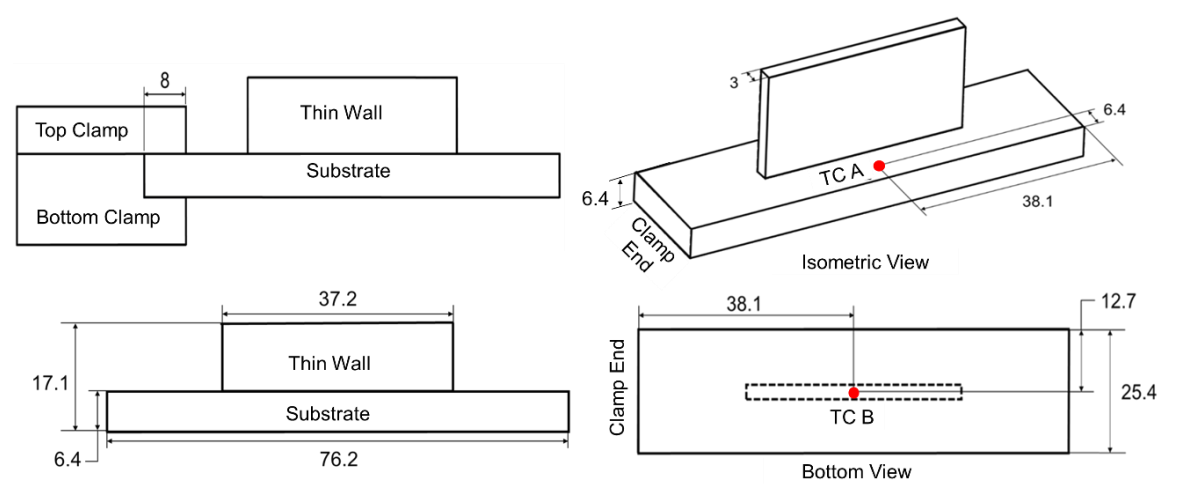


Figure 3. A schematic of the clamped substrate in relation to the thin wall. Shown also are the thermocouple locations for measuring temperature, namely, TC A for Case A and TC B for Case B.

Table 1. Process conditions for Case A and Case B reported in Ref. [19, 20].

Table 1. I focess conditions for case 11 and case B reported in Ref. [19, 20].						
Case	Case A	Case B				
Measured Laser Power (P) [W]	415	410				
Laser scan speed (V) [m×s ⁻¹]	8.5 ×	<10-3				
Powder delivery rate [g×s ⁻¹]	5 ×]	10-2				
Number of Layers	62	2				
Programmed dwell time between layers [s]	20	0				
Wall height [m]	10.7 ×10 ⁻³	11.2 ×10 ⁻³				
Measured wall length [m]	37.2 ×10 ⁻³	39.2 ×10 ⁻³				
Measured wall width [m]	2.2 ×10 ⁻³	3.0 ×10 ⁻³				
Measured Layer thickness [m]	1.7 ×10 ⁻⁴	1.8 ×10 ⁻⁴				
Laser spot size [m]	1.5 ×	1.5 ×10 ⁻³				
Distance between the nozzle tip and top of substrate - Standoff Distance [m]	11.4	11.4 ×10 ⁻³				
Approximate Build Time [minutes]	26	5				

Case A: Thin wall built with a programmed 20-second dwell time between layers.

The thin wall part is built with a programmed 20-second dwell time between the deposition of each layer. The 20-second dwell time refers to the added pause after the laser has reached the start position of the next layer before the deposition is initiated. During this period, the laser is not sintering the passing powder. The added dwell time between each of the 62 layers in Case A results in a total build time of approximately 26 minutes, which is substantially longer than the 5 minute build time of Case B, which is described below.

Case B: Thin wall built without programmed dwell time.

The thin wall part is deposited without any programmed dwell time. However, there is an inherent pause of 3 seconds between the end of one layer and the beginning of the next as the deposition head repositions to the subsequent layer's origin. In our simulations, we have included this inherent process-related dwell time of 3 seconds between layers. The build time for Case B is reported to be approximately 5 minutes.

3.2 Temperature Measurements

Temperature measurements were acquired using two Omega GG-K-30 type K thermocouples. In Figure 3, the thermocouple marked TC A is used for thin wall Case A and is located on the top surface of the substrate. The second marked TC B, used for thin wall Case B, is located at the center of the bottom surface of the substrate. These thermocouples are spot welded to the substrate and aluminum foil tape is used to shield the top thermocouple (TC A) from forced convection effects. The respective temperature signatures are shown in Figure 4.

The 20-second dwell time in Case A results in a pronounced cyclical trend in the temperature signature. The difference in dwell time allows the part in Case A to cool longer before the deposition of new layers, which reduces the peak temperature to 200 °C for Case A, compared to nearly 500 °C for Case B. The small-scale fluctuations in temperature in both Case A and B (Figure 4) are caused by the laser moving across the build, layer by layer. The local maxima occur when the laser is heating the part, and the local minima occur when the laser disabled during the programmed dwell period.

Further, because Case A had a 20-second dwell time between layers, large fluctuations in temperature are observed as significant cooling occurs between layers. In practice, such steep temperature gradients may lead to interlayer delamination in the part. In this work, the dwell time was added to test the ability of the model to respond to process changes. We note that no delamination or interlayer gaps were observed in the part used for Case A. Case B shows similar rapid cooling behavior, however because the dwell time between layers is shorter (3 seconds), the temperature fluctuations between layers is less pronounced.

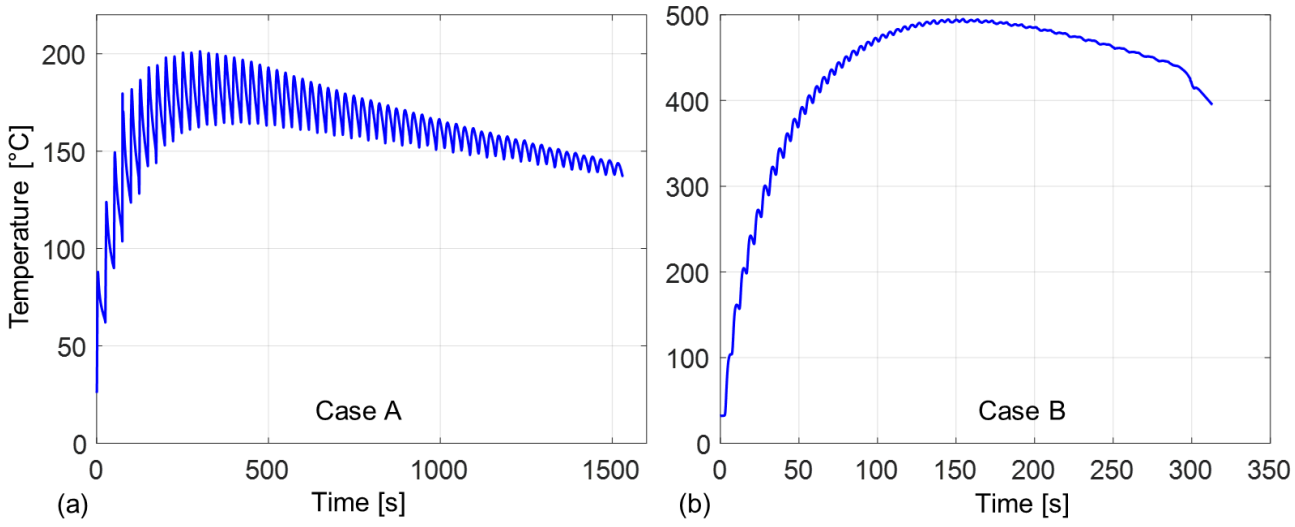


Figure 4: The temperature signatures obtained for the two thin wall cases from the thermocouple measurements. Case A has a 20-second dwell time between layers, while Case B has a 0-second dwell time programed between layers.

The gradual decline towards the end of both builds A and B is explained as follows. As each layer is deposited, the distance between the current deposited layer and point of measurement in the substrate increases, and convective and radiative heat losses dominate conductive heat transfer to the substrate. In addition, energy from the laser diffuses over a greater distance as the part builds, reducing the intensity of thermal energy applied to the thermocouple as the build progresses. Finally, the increased thermal mass of the part later in the build also damps temperature fluctuations.

In the experiments herein, absolute temperature is obtained at a single point with a thermocouple. While a thermal camera can provide thermal measurements over a larger area, the temperature reported by a thermal camera are *relative trends*, and not absolute temperature. In addition, the movement of the part relative to the fixed position of an infrared camera in DED machines is liable to cause image blurring, which is further exacerbated as the part grows in size. Hence, the preferred measurement approach for tracking the thermal history in DED is to use a thermocouple embedded inside the part or on the substrate. The tradeoff is that the thermocouple only provides a single point temperature measurement [40, 41].

Finally, we note that the graph theory model is focused on obtaining the part-level temperature distribution. The part-level temperature distribution is the key to predicting distortion from thermal-induced residual stresses. On the other hand, meltpool-level thermal distribution is important for predicting the part-level microstructure. In other words, the focus of this work is to quickly determine the global part thermal history with reasonable accuracy, and not the local meltpool temperature distribution.

4 Thermal Modeling in Additive Manufacturing using Graph Theory

4.1 Background

The graph theory approach was previously applied to predict the thermal history of parts manufactured using the laser powder bed fusion (LPBF) metal AM process [16-18]. However, certain heat transfer-related assumptions made in the context of the LPBF process to aid computation in our previous work must be altered for the DED process [16]. Figure 5 outlines the salient thermal phenomena in DED [42]. In Figure 5 the phenomena labeled 3, 4, and 5 are present in DED (including wire-arc and powder DED) and are not commonly present in other metal-based AM processes, such as LPBF.

For example, as shown in Figure 5, unlike in LPBF the part in DED is surrounded not by metal powder but by an inert gas. As a result, heat is transferred to the surroundings through convection and radiation from all surfaces. Convection in DED involves both free and forced convection, as the metal powder is delivered to the substrate via a flowing inert carrier gas, such as Argon in this work. In LPBF, the non-sintered powder acts as an insulating medium and drastically slows heat loss from the sides of the part. Hence, heat loss in LPBF predominantly occurs on the top surface of the part through radiation, free and forced convective heat transfer at the meltpool [43-45]. Heat loss in the rest of the LPBF part occurs largely through conduction, although heat loss through free convection occurs at the part-powder boundaries through air gaps in the surrounding powder.

In the context of Figure 5, LPBF heat losses from the substrate driven by the 5th (free convective heat transfer) and 6th (conduction) phenomena would be negligible in practice. Consequently, for a comprehensive model of part-level thermal history in DED, it is necessary to account for heat loss through conduction, free and forced convection, and radiation. Accordingly, in the present work, a combination of free and forced convection regimes are considered for

modeling the DED process. As will be explained in Sec. 4.3, heat loss due to forced convection is assumed for all part surfaces over which there is a predominant flow of carrier gas. Heat loss due to free convection is assumed at surfaces that are not directly affected by the carrier gas, such as the bottom and sides of the substrate.

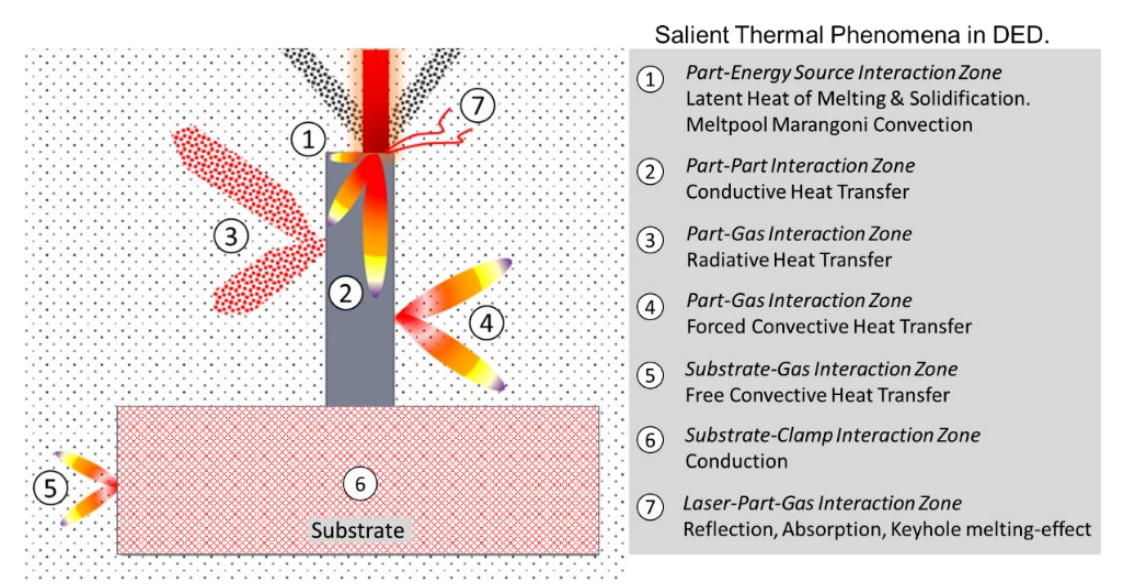


Figure 5. Salient thermal phenomena in DED include conductive, convective, and radiative heat transfer. Phenomena labeled 3, 4, 5, are largely absent in LPBF.

Furthermore, the laser heat source-related assumptions in LPBF do not carry over to the DED process because the scan velocity and spot size (beam diameter) of the laser, volumetric rate of material deposition, and layer thickness are considerably different [44, 46]. In LPBF, movement of the laser is achieved using a pair of electrically controlled mirror galvanometers. By contrast, in DED, the laser head is translated by the physical motion of CNC-based axes. Consequently, the scan velocity of the laser in DED is many times slower compared to LPBF – the scan speed of the laser in LPBF is typically 200 to 1000 mm·s⁻¹; In DED, the scan speed is on the order of 10 mm·s⁻¹. Further, the typical layer thickness is around 50 μm in LPBF, compared to ~100 μm to 200 μm for DED. Lastly, the laser beam diameter in the DED process is typically nearer to the 500 μm range compared to ~50 μm to 100 μm in LPBF [46].

From a thermal modeling perspective, the higher laser scan velocity and smaller layer thickness of LPBF are advantageous for reducing computation time. Researchers often simulate the deposition of multiple layers at a time in LPBF (called the super-layer or meta-layer assumption) to reduce computation time [47, 48]. For example, Williams *et al.* [47] used the meta-layer assumption in an FE-model to predict thermal-induced deformation in LPBF. Meta-layers ranging from 12 to 50 times the actual layer thickness (50 µm) are simulated. Williams *et al.* [47] showed that their model predicts distortion within 5% of measurements, despite simulating the deposition of ~15 layers simultaneously. The slow scan speed and large laser spot size of DED creates a meltpool which has a large diameter and penetrates deeper into the previous layers compared to LPBF. Consequently, the super-layer assumption is not viable in DED. Moreover, in our previous work applying graph theory for thermal modeling in LPBF, the laser was considered as a point source of heat [16-18]. In the current work, the double ellipsoid model originally developed by Goldak is used to approximate the shape, temperature, and depth of penetration of the meltpool [49, 50].

4.2 The graph theory solution to the heat diffusion equation

To predict the temperature distribution, it is necessary to solve the continuum *heat diffusion equation* [51]. In DED, and in metal AM in general, FE analysis is used to solve the heat diffusion equation and obtain the temperature history [52].

Material Properties
$$\frac{\partial T(x,y,z,t)}{\partial t} - k \underbrace{\left(\frac{\partial^2}{\partial x^2} + \frac{\partial^2}{\partial y^2} + \frac{\partial^2}{\partial z^2}\right)}_{Laplacian} T(x,y,z,t) = \underbrace{\widetilde{E_V}}_{Input Energy Density}$$

$$\text{where } E_V = \frac{P}{vht}$$

In Eqn. (1), T is the temperature rise above the ambient temperature. Solving the heat diffusion equation with the accompanying boundary conditions (shown in Eq. (2)) results in the temperature

T(x, y, z, t) at a location (x, y, z) at a time at instant t, which is the thermal history for a part. The term E_V , called energy density $[J \cdot m^{-3}]$, is the energy supplied by the laser to melt a unit volume of material. The energy density $E_V = \frac{P}{vht}$ is a function of laser power (P) [W], distance between adjacent passes of the laser (h) [m], relative translational velocity of the part (v) [m·s⁻¹], and the layer thickness (t) [m]; These are the controllable parameters of the process. The material properties required to solve this equation are density ρ [kg·m⁻³], specific heat c_p [J·kg⁻¹·K⁻¹], and thermal conductivity k [W·m⁻¹·K⁻¹].

The accompanying initial and boundary conditions are given by,

$$T(x, y, z, 0) = T_a \text{ (initial condition)}$$

$$\frac{\partial T}{\partial n} = 0 \text{ (on boundary)}$$
(2)

where n is the outward normal vector at the boundary and T_a is the ambient temperature of the environment. Although this boundary condition is for zero heat loss, the effect of external heat loss by convection and radiation is implemented later as an adjustment to the graph theory method and is discussed in Sec. 4.3.

Part shape is embedded in the heat equation through the second derivative term, called the *Continuous Laplacian*. The graph theory approach reduces the computational burden by solving a discrete version of the heat diffusion equation, which eliminates the meshing steps of FE analysis.

As with existing FE approaches, the laser energy density E_V in Eq. (1) is replaced by an initial temperature distribution caused by the laser, $T_o(x, y, z)$. An estimate of the laser power needed to raise the metal temperature from ambient T_a to the initial temperature is given by an energy balance, as follows:

$$\rho vhtc_p(T_o - T_a) = P$$

$$\therefore (T_o - T_a) = \frac{P}{c_n \rho vht}$$
(3)

Here ρvht is the rate of mass deposited [kg · s⁻¹]. Then the heat diffusion equation and the accompanying conditions become,

$$\frac{\partial \mathbf{T}}{\partial t} - \alpha \left(\frac{\partial^2}{\partial x^2} + \frac{\partial^2}{\partial y^2} + \frac{\partial^2}{\partial z^2} \right) \mathbf{T} = 0 \tag{4}$$

 $T(x, y, z, t = 0) = T_o(x, y, z)$ (initial condition)

$$\frac{\partial \mathbf{T}}{\partial n} = 0 \quad \text{(on boundary)} \tag{5}$$

where $\alpha = k/(\rho c_p)$ is the thermal diffusivity, α [m²·s⁻¹]. The boundary condition T_o depend on the shape and temperature of the meltpool and is estimated using Goldak's double ellipsoid model, described in Sec. 4.3.3.

Next, the heat diffusion equation is discretized over N nodes by replacing the negative continuous Laplacian with the discrete *Laplacian matrix* (L):

$$\frac{\partial \mathbf{T}}{\partial t} + \alpha \mathbf{L} \mathbf{T} = 0; \tag{6}$$

The eigenvector matrix (ϕ) and eigenvalue matrix (Λ) of the Laplacian matrix (L) are found by solving the eigenvalue equation $L\phi = \phi\Lambda$. As the Laplacian matrix is symmetric and positive semi-definite, as described later in Sec. 4.3, the eigenvalues (Λ) are non-negative, and the eigenvector matrix (ϕ) is orthogonal [53-56]. Because the transpose of an orthogonal matrix is the same as its inverse, that is, $\phi^{-1} = \phi'$ and $\phi \phi' = I$, where I is the identity matrix, then the eigenvalue equation $L\phi = \phi\Lambda$ may be post-multiplied by ϕ' to obtain $L = \phi\Lambda\phi'$. Substituting $L = \phi\Lambda\phi'$ in Eqn. (6) gives:

$$\frac{\partial \mathbf{T}}{\partial t} + \alpha(\phi \Lambda \phi') \, \mathbf{T} = 0; \tag{7}$$

Eqn. (7) is a first order, ordinary linear differential equation, with solution [61],

$$T = e^{-\alpha(\phi \Lambda \phi')t} T_o$$
 (8)

The term $e^{-\alpha(\phi \Lambda \phi')t}$ is simplified via a Taylor series expansion and substituting $\phi \phi' = I$,

$$e^{-\alpha(\phi \Lambda \phi')t} = \phi e^{-\alpha(\Lambda)t} \phi' \tag{9}$$

Substituting, $e^{-\alpha(\phi \Lambda \phi')t} = \phi e^{-\alpha \Lambda t} \phi'$ into Eqn. (8) gives,

$$T = \Phi e^{-\alpha \Lambda t} \Phi' T_o \tag{10}$$

Eqn. (10) is the graph theory solution to the discrete heat diffusion equation as a function of the eigenvalues (Λ) and eigenvectors (Φ) of the Laplacian matrix (L), constructed on a discrete set of nodes. The graph theory approach has two inherent advantages over FE analysis, (i) elimination of mesh-based analysis; And (ii) Elimination of matrix inversion steps. To explain further, while FE analysis requires matrix inversion at each time-step for solving the heat diffusion equation, the graph theory approach relies on matrix multiplication and transposes, shown in Eq. (9), which greatly reduces the computational burden.

4.3 Application of the Graph Theory Approach to Thermal Modeling of the DED Process

4.3.1 Steps in the Approach

The graph theory approach as applied to the DED process is explained in the context of Figure 6. The initial inputs to the model are as follows:

- Part geometry: Part shape in .stl form; hatch (bead) thickness, spacing and width; direction of deposition.
- Processing parameters: laser power (P) (for obtaining meltpool temperature) and velocity (V),
 dwell time between layers.
- Material Properties: specific heat (Cp); thermal conductivity (k); thermal diffusivity (α)
- Model parameters: block size and number of nodes,

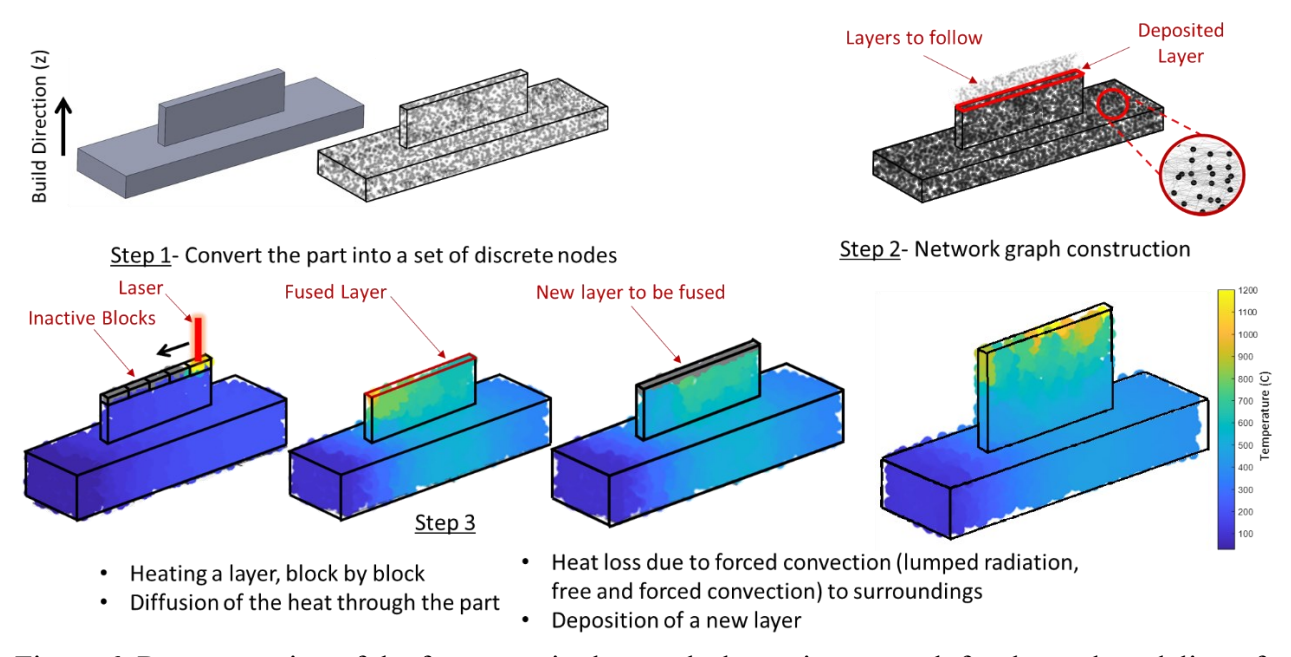


Figure 6. Representation of the four steps in the graph-theoretic approach for thermal modeling of the DED process.

Step 1: Hatch-by-hatch discretization of the part geometry.

The process is simulated hatch-by-hatch (bead by bead). For this purpose the size (shape, length, breadth, and height) and direction of the hatch is taken into consideration. Each hatch is further divided into discrete blocks (volumes) with a fixed height and length, with breadth equal to the actual hatch width. The discretization of the process into hatches is shown in Figure 7.

In the DED process, the laser travel is a continuous motion problem. To simplify the motion of the laser to aid calculation speed, the single track or hatch that composes each deposited layer were broken into five equal size blocks. In this work, the block size is chosen to match with the dimensions of the part. These discrete blocks are 7.84 mm long, 3 mm wide, and 0.1806 mm thick in this work. The width of the block is equal to the width of an ideal deposited hatch, and its thickness is equal to the layer thickness. This block-by-block progress of the DED process is similar to the inactive element technique used in FE simulations which are currently used by commercial software [21, 32, 51]. Since the laser scan velocity is 8.5 mm·s⁻¹ and the length of each block is 7.84 mm long, the time to step between blocks is 0.922 s.

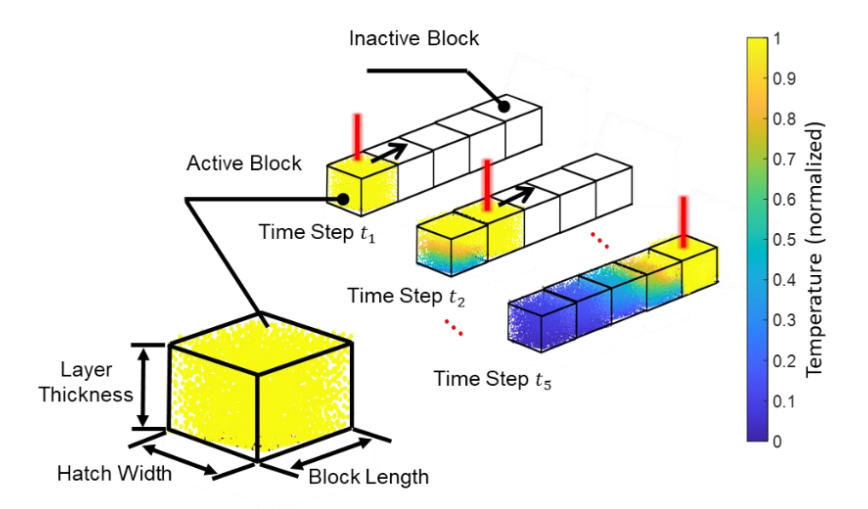


Figure 7. Hatch-by-hatch (bead-by-bead) build scheme used in DED simulation using graph theory. Each hatch is discretized into blocks, and each block is further discretized into nodes. Each block is the same height as the layer thickness, and the block width is equal to the bead width. The blocks are added in the direction of the hatch, thus the size of the hatch and its build direction are taken into consideration.

The deposited part is composed of 310 blocks while the substrate is formed by 2520 blocks for a total of 2830 blocks in the model. By keeping each block of identical size, the effective energy applied is consistent across the newly fused layer. Each block is randomly populated with N number of nodes. The number of nodes per unit volume (called node density) is uniform throughout. The number of nodes is analogous to the size of elements in the context of FE analysis. In the finite element method, increasing the number of elements by decreasing element size increases the model precision, and a sequence of model solutions will converge to a 'best' solution. If the element size becomes too large, the solution will provide poor precision.

In a similar sense, a large node density results in the part being discretized using more nodes, thus improving the convergence accuracy albeit, at the tradeoff of computational time. In this work we test the effect of node density at three levels. The three node densities are tested for Case A and Case B, these are: 0.235 nodes·mm⁻³, 0.470 nodes·mm⁻³, and 0.706 nodes·mm⁻³. As will be reported in Sec. 5, in the context of Figure 12 and Table 7, these tested node densities converged to an appreciable degree to the experimental data, with the node density of 0.706 nodes·mm⁻³ providing the most accurate prediction. The discretization process results in each node having a unique Cartesian (x, y, z) coordinate, i.e., the location of each node is spatially defined within the part.

When the laser heats a block, all of its nodes appear at the same time. The justification for this is to simulate the material deposition when the deposition head is above the block. In this representation of the DED process, making the blocks smaller will improve the simulation accuracy of the model at the expense of computation time. Since the nodes are populated in a

random manner, there is a degree of stochasticity in the model predictions. We quantify this uncertainty by repeating the simulations three times for each case.

Step 2: Constructing a network graph from the cloud of discrete nodes created in Step 1.

Each node is connected to its nearest neighboring nodes within a radius (ϵ). Consider ϵ [mm] as describing the radius of a sphere with a node at its center. Nodes that fall within the volume of the sphere are connected to the node at the center of the sphere. Nodes that are outside of the sphere are not connected. This step is completed throughout the entire cloud of nodes, which results in a complex web of connections called a network graph.

Consider two nodes, π_i and π_j , whose spatial Cartesian coordinates are $c_i \equiv (x_i, y_i, z_i)$ and $c_j \equiv (x_j, y_j, z_j)$, respectively; π_i and π_j are connected by an edge having weight $a_{i,j}$ if the distance between them is less than ϵ . The distance between π_i and a node π_j whose spatial Cartesian coordinates $c_j \equiv (x_j, y_j, z_j)$ is the Euclidean distance $\|c_i - c_j\| = \sqrt{(x_i - x_j)^2 + (y_i - y_j)^2 + (z_i - z_j)^2}$. The edge weight $a_{i,j}$ is given by,

$$a_{i,j} = \begin{cases} e^{-\frac{\left\|c_i - c_j\right\|^2}{\sigma^2}} \text{if} \left(c_i - c_j\right)^2 \le \varepsilon \\ 0 \text{ otherwise} \end{cases}$$
 (11)

In Eqn. (11), σ is the standard deviation of all the pairwise distances between nodes, and the exponential term is the Gaussian function that scales the pairwise distance between the nodes in the part between 0 and 1. The neighborhood distance ε is a heuristic tunable parameter in the graph theory model that needs to be calibrated (only once) for a material type. The calibration procedure for ε is described in Sec. 4.3.4.

The matrix formed by calculating a_{ij} is called the adjacency matrix, $A = [a_{ij}]$, which is a positive symmetric matrix.

$$\mathbf{A} = \begin{bmatrix} 0 & a_{1,2} & a_{1,3} & \cdots & a_{1,N} \\ a_{2,1} & 0 & a_{2,3} & \cdots & a_{2,N} \\ a_{3,1} & a_{3,2} & 0 & \cdots & a_{3,N} \\ \vdots & \vdots & \vdots & \ddots & \vdots \\ a_{N,1} & a_{N,2} & a_{N,3} & \cdots & 0 \end{bmatrix}$$
(12)

From the adjacency matrix, the degree h_i of a node π_i is calculated by summing the corresponding i^{th} row (or column) of A. The degree matrix (H) is obtained in the following manner.

$$h_{i\cdot} = \sum_{j=1}^{N} a_{i,j}$$

$$H = \begin{bmatrix} h_{1\cdot} & 0 & 0 \\ 0 & \ddots & 0 \\ 0 & 0 & h_{N\cdot} \end{bmatrix}$$
(13)

In the degree matrix H, all the off-diagonal entries are zero and the diagonal entries d_i are positive. The graph Laplacian at node π_i is defined as: $L_{ij} \stackrel{\text{def}}{=} h_i - a_{ij}$, and the Laplacian matrix is obtained $L = [l_{ij}]$. The discrete graph Laplacian matrix is as follows:

$$L = \begin{bmatrix} +h_{1} & -a_{1,2} & -a_{1,3} & \cdots & -a_{1,N} \\ -a_{2,1} & +h_{2} & -a_{2,3} & \cdots & -a_{2,N} \\ -a_{3,1} & -a_{3,2} & +h_{3} & \cdots & -a_{3,N} \\ \vdots & \vdots & \vdots & \ddots & \vdots \\ -a_{N,1} & -a_{N,2} & -a_{N,3} & \cdots & +h_{N} \end{bmatrix}$$

$$(14)$$

Finally, the Eigenspectra of the graph Laplacian matrix (L) will be computed as $L\varphi = \Lambda\varphi$, where φ are the eigenvectors and Λ are the eigenvalues of L [57].

Step 3: Block-by-block simulation of a layer

Figure 7 demonstrates the block-by-block heating scheme used in this work to discretize the continuous motion of the laser. The DED simulation progresses by heating the nodes in a block, before proceeding to the nodes in the next block. Constant heat input was maintained by only heating one block at any time. In other words, a time step involves heating of nodes inside a block, one block at a time.

Step 3(a): Heat loss through conduction

After a block is heated by the laser, the heat is allowed to diffuse through the network graph that was constructed in Step 2. Conduction is the sole mode of heat transfer between the nodes. The only active nodes during this step are located within layers and blocks that have already been deposited. Other nodes that are in subsequent blocks and layers remain inactive and, therefore, are unable to transfer heat. After the heat diffuses from the block previously heated by the laser, the deposition of the next block is simulated. This process is repeated for every block and every layer in the part.

The mathematical implications of the approach will be summarized here by only including the final derived equation, shown in Eqn. (15). After the time required to heat each block, in this case $t_b = 0.922$ s, has passed, the temperature of each active node is stored in the temperature matrix T_b .

The temperature following heat loss through conduction (T_c) is defined as a function of the Laplacian eigenvectors (ϕ) and eigenvalues (Λ) of the network graph of active nodes, where T_0 is the meltpool temperature, and g is a tunable parameter called the gain factor. The gain factor (g) scales the rate of thermal diffusivity or heat flux between nodes. A higher gain factor increases the rate of thermal diffusion through the part, i.e., the larger the gain factor, the faster the heat will dissipate through the part by conduction. The procedure to calibrate the gain factor is reported in Sec. 4.3.4.

$$T_c = \Phi e^{-\alpha g \Lambda t_b} \Phi' T_0 \tag{15}$$

Step 3(b): Heat loss through convection

To accommodate the heat loss through convection and radiation, these terms were combined into a single forced convection term and were applied using Newtons law of cooling on the identified surface boundary nodes. The approach is as follows.

Heat loss through conduction between the nodes is followed in tandem with heat loss through forced and free convection from the nodes on the surface of the part. The temperature distribution after heat loss through forced and free convection, and through clamp conduction, takes place for the duration of the time t_b , and is calculated as,

$$T_b = T_c e^{-\beta t_b}$$

$$\beta = \frac{h}{\rho L C_p}$$
(16)

Where h is the heat transfer coefficient [W·m⁻²·K⁻¹], ρ is the material density [kg·m⁻³], and L (= 7.84 ×10⁻³ m) is the length of the block, and C is the specific heat [J·kg⁻¹· °C⁻¹] which is not a constant, but temperature-dependent in this work. The derived coefficient, β , is called the inverse time constant [s⁻¹]. The heat transfer coefficient h has two parts, to include both free and forced convection. Heat loss due to forced convection is applied to the sides of the part and top of the substrate as the carrier argon gas flows over these surfaces. Free convection is dominant on the sides and bottom of the substrate, where there is no active gas flow. The heat transfer coefficients are discussed in depth in Sec. 4.3.4.

In Steps 3(a) and 3(b), for simplicity, we described the heating of only those blocks in the topmost layer. However, in DED the block in the prior layers immediately below the block being currently heated is also at an elevated temperature as the laser penetrates the existing part. The

heating of nodes in the blocks immediately below an actively heated block on the top layer is implemented using Goldak's double ellipsoid model, detailed in the forthcoming Sec. 4.3.2.

Step 3(c). Obtaining the temperature at the end of a layer after dwell time.

For each block-by-block iteration of step 3(a) and (b), the temperature of every node is recorded in a vector T_b . This is repeated until an entire layer is simulated. After the process reaches the end of the layer, heat is allowed to dissipate by conduction immediately followed by convection in time steps of 1 second, iteratively for a period equal to the dwell time (t_d). Different size time steps have previously been explored for the spectral graph method in our related work [17].

For this work, based on extensive offline studies, a time step of 1 second provided adequate precision. In this work, t_d was 20 seconds for Case A, and 3 seconds for Case B. Therefore, Eqs. (17) and (18) were iterated 20 times for Case A and 3 times for Case B with time t=1 s to simulate the total dwell time between layers.

$$T_{Lc} = \Phi e^{-\alpha g \Lambda t} \Phi' T_b \tag{17}$$

$$T_{Lf} = T_{Lc}e^{-\beta t} \tag{18}$$

Step 4: Steps 3(a), (b), and (c) are looped until the last layer is built. The temperature of each node at each time step is recorded in a vector T, which contains the thermal history of the part.

4.3.2 Model Assumptions

The spectral graph method involves some additional simplifying assumptions because the method is built on the solution of a linear differential equation. These assumptions are common in FE-based part level thermal modeling in AM, including LPBF and DED [51]. First, it is assumed that material properties, such as density (ρ) , do not change as the material changes state from particulate matter to a liquid (meltpool formation) then back to a solid. This assumption allows the

use of effective (average) values of the properties. Second, the latent heat of melting and solidification is not included in the model. However, in keeping with literature, the thermal diffusivity of the material (α , a function of specific heat C_p and conductivity, k) is considered to be temperature dependent.

Lastly, a common practice in the thermal modeling literature in AM is to assume that the thermal gradients are decoupled from the mechanical response (part deformation) [51]. To explain further, the thermal simulation of AM parts, including LPBF and DED, are conducted over several time steps. The thermal history predictions over this longer horizon are then used to estimate the mechanical response [47, 58-64]. The thermal and mechanical aspects are thus considered independent (decoupled); While the thermal history influences the mechanical response, the mechanical response is assumed to have no effect on the thermal response. This assumption has its genesis in the computational thermomechanics of welding literature, as detailed by Goldak and Alkhaghi [50]. Commercial thermal simulation software such as Autodesk Netfabb, Amphyon, Simufact, and Additive Print implement the decoupled modeling approach [65].

The benefit of decoupled thermomechanical modeling is that the computation is more efficient than a coupled thermomechanical approach while providing reasonable prediction accuracy. However, the decoupled thermomechanical model loses fidelity when the distortion is sufficiently severe to change boundary conditions. Based on small deformation theory, as elucidated by Michaleris and co-workers [51], this decoupling assumption is valid when there are no major faults, such as severe cracking or separation of the part from the build plate. Such failures would not only alter the shape of the part but also change the heat conduction pathway, leading to considerable changes in the temperature profile. In other words, a change in boundary conditions can result from substantial change in the shape of the part which fundamentally changes the

thermal conduction pathway. This work assumes the thermal and mechanical responses are decoupled.

4.3.3 Modeling the Laser Heat Source using Goldak's Double Ellipsoid Model

As depicted in Figure 8, in DED, not only is the current layer processed by the laser at an elevated temperature but also material in prior layers below the laser path is reheated. Therefore, apart from considering only the nodes at the surface at a higher temperature, T_0 , it is necessary to initiate the sub-surface nodes with an elevated temperature.

The temperature at the surface as well as the temperature of prior layers is a function of the material properties and meltpool temperature. Goldak's double ellipsoid model in Eqn. (19) is used to quantify the temperature reached by the sub-surface nodes [49, 50, 66],

$$T_0(x, y, z, t) = C \cdot P \frac{1}{2\pi k \sqrt{x^2 + y^2 + z^2}} e^{-\frac{V}{2\alpha} \times (x + \sqrt{x^2 + y^2 + z^2})}$$
(19)

In Eqn. (19), $T_0(x, y, z, t)$ is the temperature at time t on account of the heat supplied by the laser; x, y, and z are local coordinates of the meltpool. P is the laser power, k is the thermal conductivity, and C is a dimensionless scaling factor. The laser velocity and thermal diffusivity are represented by V and α , respectively. Each variable is defined with the appropriate values and units in Table 2. The scaling factor C effects the meltpool temperature; Figure 9 demonstrates the effect of the scaling factor as a function of the meltpool location along the x-axis, with y = 0 and z = 0.

A characteristic of the model is that the temperature asymptotes to infinity at the center of the meltpool. The meltpool temperature is taken as the intersection of the vertical line drawn from the trailing edge of the beam (x = -0.75 mm) with the temperature curve. In this work, the liquidus

temperature for Ti-6Al-4V is assumed to be 1630 °C. Based on the literature, we demarcate three meltpool temperatures (T_0), namely $T_0 = 1900$ °C, $T_0 = 2200$ °C, and $T_0 = 2450$ °C.

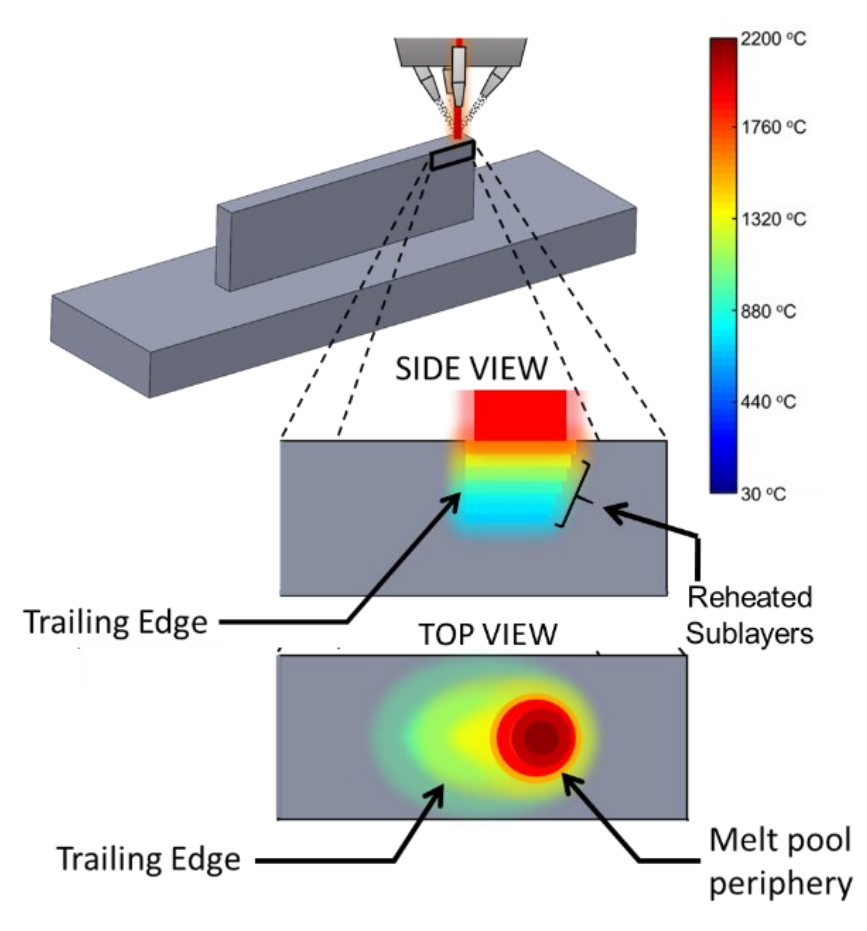


Figure 8: The effect of meltpool temperature on the sub-surface layers, and the periphery of the meltpool.

Table 2. Variable definitions for Equation (19) [19, 20].

Variable	Units	Value
С	Dimensionless	0.125 to 0.191
Laser Power (P)	[W]	415
Laser Velocity (V)	[m·s ⁻¹]	8.5×10^{-3}
Thermal Conductivity (k)	[W·m ⁻¹ K ⁻¹]	6.8
Thermal diffusivity (α)	$[m^2 \cdot s^{-1}]$	2.7228×10^{-6}

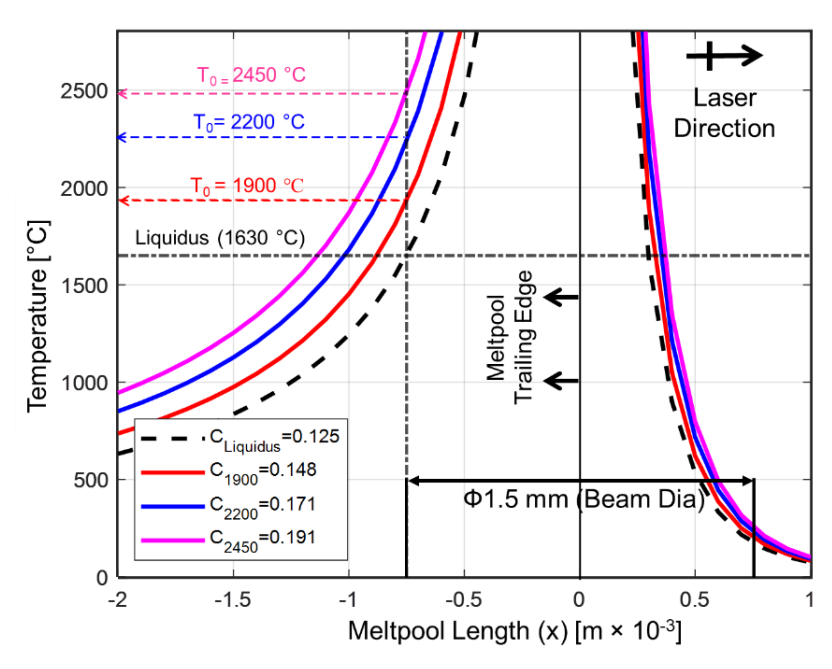


Figure 9. The effect of the scaling factor C on the meltpool temperature, as a function of the meltpool length.

Various researchers estimate the average meltpool temperature in the processing of Ti-6Al-4V in the region of 2000 °C to 2100 °C (Table 3). The literature shows that the meltpool temperature in DED of Ti-6Al-4V exceeds melting temperature of the material (~1630 °C). Hence, three different meltpool temperatures are considered in this work and shown in Figure 9: 1900 °C, 2200 °C, and 2450 °C, which represent the range of meltpool temperature values observed and measured in the literature. We note that researchers have also observed that small areas of the meltpool can reach superheating temperature [67-69].

To estimate the sub-surface depth penetrated by the laser, we plot Eqn. (19) as a function of the depth (z), with x = 0, and y = 0 starting from the middle of the top layer; The sub-surface temperature curves for different values of the scaling factor C (meltpool temperature) are shown in Figure 10. For simulation purposes, we only consider blocks up to a depth immediately below the current block and whose temperatures reach at least 20% of the liquidus temperature (1630)

°C). For the various curves, the temperature reaches 326 °C (20% of the liquidus) around the seventh sub-layer, approximately 1.25 mm below the top surface.

Table 3. Summary of meltpool temperatures found by other researchers in the literature.

Geometry	Geometry Laser Scan		Method	Meltpool	Ref.
	Power (P)	Velocity (V)		Temperature	
	[W]	$[\text{mm}\cdot\text{s}^{-1}]$		(T_0) [°C]	
Thin Wall	300	12.7	Pyrometer	~1850	[70]
Single Track	2000	10.6	Thermocouple	1865 ± 190	[71]
Thin Wall	290	12.7	Pyrometer	1900-2000	[68]
L-shaped Thin Wall	450	10.6	IR Camera	2485 ± 161	[72]
Cylinders	350	16.9	Pyrometer	2100 - 2500	[67]
Rectangular Thin Wall	300	2.0	Quiet Element FE	~2450	[73]
Cube	800	10.0	In-house FE Code	2500	[74]
Thin Wall	425	8.5	Inactive Element FE	1800 - 2000	[21]

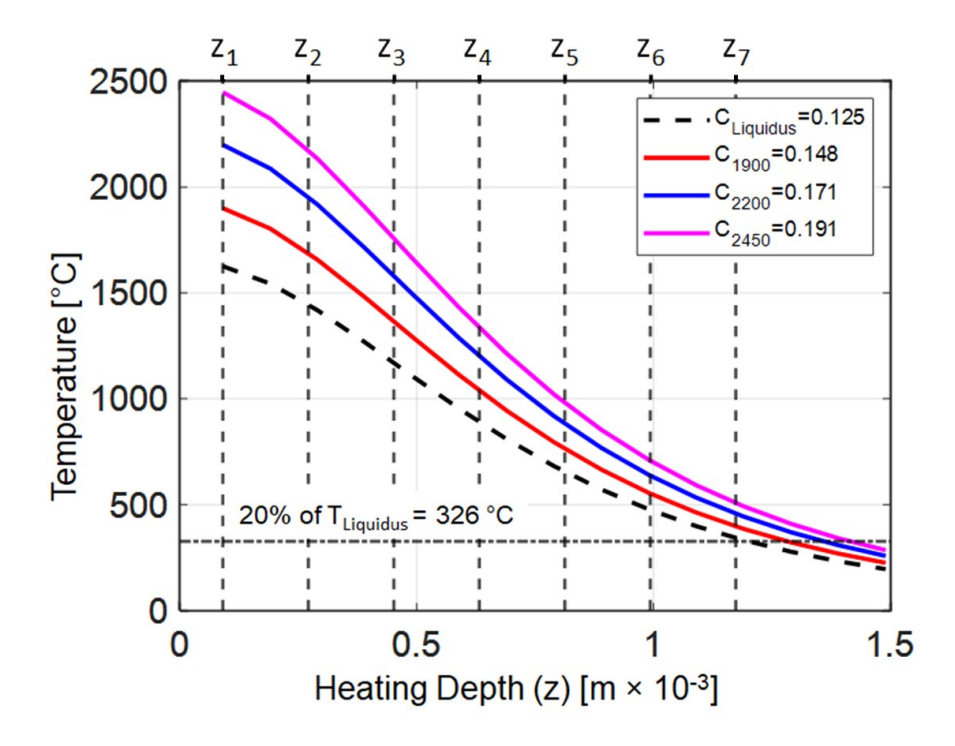


Figure 10: The temperature reaches 20% of the liquidus at a depth of 1.25 mm from the top surface.

4.3.4 Heat Loss due to Radiation and Convection, and Model Calibration

(a) Calibrating Model Parameters ε and g

Case A was used for calibrating the parameters of the graph theory method, namely, the neighborhood size (ε) and gain factor (g) in Eqn. (15) and Eqn. (17). Case A was chosen for calibration given the prominent temperature cycles, as evidenced in Figure 4. An iterative grid search was performed to calibrate the gain factor and neighborhood size. The combination of neighborhood size and gain factor that resulted in the lowest Mean Absolute Percentage Error (MAPE) in Case A was selected and subsequently applied without any modification for Case B. This calibration process was repeated for different node densities and meltpool temperatures based on Case A and held constant thereafter. In other words, these simulation parameters need to be calibrated once for a particular material and node density.

Table 4 reports the gain factor (g) and neighborhood size (ε) that minimize the MAPE for Case A for a given density of nodes and melt pool temperature assumption. Calibration of the gain factor g was conducted at three different node densities, corresponding to one, two, and three nodes within each block. An important observation is that approximately 90% of all nodes are located in the substrate with the remaining 10% located in the actual part. This is because the volume of the substrate (12,387 mm³) is nearly 10 times as large as the part (1227 mm³). A large proportion of the computation effort is therefore required to compute the edge connections for the nodes in the substrate; Heigel $et\ al.\ [19,20]$ reduce computation time by simulating only half of the part volume while the current method simulates the entire part.

Table 4. Three node densities, and corresponding simulation parameters ε and g.

				Neigh	Gain Factor (g)			
Nodes per	Total Number	Nodes in	Nodes	Node Density	borhoo	$T_0 =$	$T_0 = 2200$	$T_0 = 2450$
Block	of nodes	Substrate	in Part	(nodes/mm ³)	d Size, ε (mm)	1900 °C (mm ⁻²)	°C	°C
					0 (11111)	(111111)	(mm ⁻²)	(mm^{-2})
1	2830	2520	310	0.2355	4.5	8	10	12
2	5660	5040	620	0.4709	4.75	1	1.5	1.95
3	8490	7560	930	0.7064	5.5	0.12	0.15	0.17

(b) Heat Transfer Coefficients

Three heat transfer coefficients in the DED simulation are fixed in the calibration step and are held constant throughout all ensuing simulation cases, irrespective of node density or melt pool temperature. Table 5 reports the heat transfer coefficients used in this work along with the corresponding salient thermal phenomena in DED that describes them in Figure 11; Values used by Heigel *et al.* are also provided for comparison purposes [19].

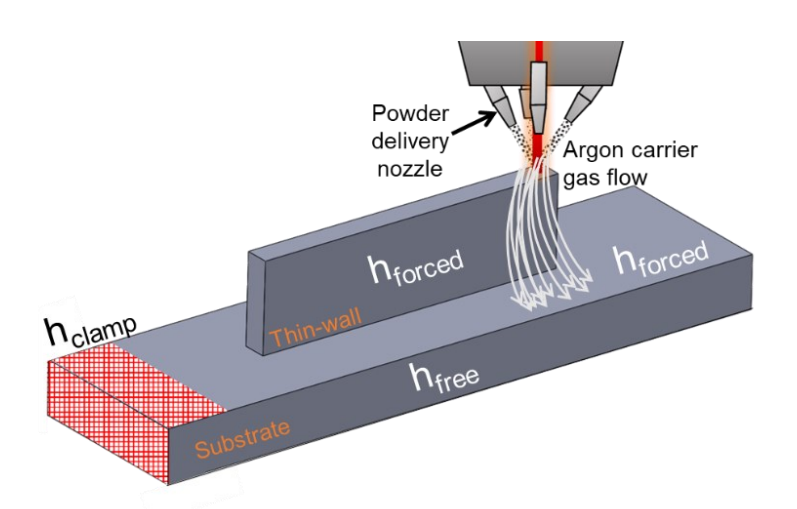


Figure 11: The portioning of the heat transfer coefficients into forced and free, and due to the clamp. The top surface of the substrate, and sides of the part are subjected to heat loss due to forced convection. The sides and bottom of the substrate loses heat on account of free convection.

Because the DED process builds new parts by moving the heat source and shielding gas, convection boundary conditions must be considered. Referring to Figure 11, argon gas in the DED process propels titanium powder particles into the laser beam and melt pool. The argon gas continues to flow down the sides of the thin wall while the deposition takes place. Although the

sides of the thin wall and top surface of the substrate experience heat loss due to forced convection, the same cannot be assumed for the sides and bottom surface of the substrate. This necessitates a separate consideration of each boundary condition and the use of two distinct heat transfer coefficients.

A forced heat convection coefficient (h_{forced}) is used to describe the forced convection loss caused by the flowing argon shielding gas on the sides of the part and top surface of the substrate. A free heat convection coefficient (h_{free}) describes the remaining free convection loss experienced at the sides and bottom surface of the substrate. The forced heat transfer coefficient is approximated as $10 \times h_{free}$. In Table 5, these heat losses are encapsulated under the broad term *heat transfer coefficients*, because, apart from conductive and convective heat transfer, heat loss also occurs through radiation. The portion of the part closest to the deposition nozzle experiences the largest heat loss due to forced convection from the carrier gas (= 60 W·m⁻²·K⁻¹), which reduces in a non-linear manner (= 25 W·m⁻²·K⁻¹) further away from the tip. In this work, the forced heat transfer is held constant ~ 50 W·m⁻²·K⁻¹.

Table 5. Equivalent heat transfer coefficients used in graph theory method.

Heat Transfer	Equivalent Heat	Corresponding Salient	Equivalent Heat Transfer
Coefficient	Transfer	Thermal Phenomena	Coefficient Value in Heigel's
	Coefficient used	(refer to Figure 5)	Model [19]
	in this work		$[W \cdot m^{-2} \cdot K^{-1}]$
	$[W \cdot m^{-2} \times K^{-1}]$		
Forced Heat Transfer Coefficient $h_{\text{forced}} \approx 10 \times h_{\text{free}}$	50	(3), (4) Radiative and forced convection heat transfer between the part and gas	60 (near the top of the wall) decreasing to 25 near the bottom of the wall
Free heat transfer	5	(5) Free convective heat	10
Coefficient		transfer between the	(on the top surface and side
h _{free}		substrate, part and gas	of the substrate)
Clamp heat loss	980	(6), Heat loss at	N/A. Only half the clamp
Coefficient		Substrate-Clamp	volume is simulated.
$h_{clamp} \approx 20 \times h_{forced}$		interface.	

The last heat transfer coefficient used is called the clamp coefficient (h_{clamp}). As previously described in the experimental setup (Figure 3), the substrate was clamped at one end. The surfaces of the substrate in contact with the clamp have an extra loss since the clamp acts as a large heat sink. Therefore, this extra thermal pathway must be considered in the simulation. Simulating the effect of the clamp by populating its geometry with nodes (in graph theory) and elements (in FE) substantially increases the computation time. We simulate the entire thin wall part and substrate, and account for the heat loss at the clamp without simulating the geometry of the clamp. This is done by assuming that the surfaces of the substrate in contact with the clamp have an elevated loss given by a coefficient that is 20 times larger than that of the forced heat loss coefficient ($h_{clamp} \approx 20 \times h_{forced}$).

The clamp heat loss is set to a large value to simulate metal-to-metal contact between the substrate and the clamp. Above $h = 100 \text{ W} \cdot \text{m}^{-2} \times \text{K}^{-1}$, the temperature of the interface approaches ambient temperature T_a , and heat conduction through the part governs heat loss from the part. As such, the exact convection coefficient for this portion of the model is not consequential, so long as it is a large value. The value 20 x h_{forced} was selected as it was much larger than any of the convection coefficients and was also large enough to ensure that the boundary in the clamp region was close to the ambient temperature, T_a , for the entire simulation.

(c) Transient Material Properties

In the current work, thermal diffusivity (α) is modeled as a function of temperature. To calculate thermal diffusivity ($\alpha = \frac{k}{\rho C_p}$), we use the values of thermal conductivity (k) and specific heat (C_p) values in Table 6 provided by Heigel *et al* [19, 20]. For all calculated thermal diffusivity values presented in the table, a density (ρ) = 4.43 × 10³ [kg·m⁻³] was used for Ti-6Al-4V.

A linear function with temperature as the independent variable is fitted to the α values. At the end of a layer, the average temperature of the layer after deposition (\bar{T} [°C]) is obtained, from which the thermal diffusivity value for the next layer ($\alpha(\bar{T})$) is ascertained. The linear equation is $\alpha(\bar{T}) = 0.0042\bar{T} + 2.612$. The density of the material is considered to be constant.

Table 6. Temperature-dependent thermal properties for Ti-6Al-4V from Ref. [19, 20].

T [°C]	$k \left[\mathbf{W} \cdot \mathbf{m}^{-1} \cdot {}^{\mathrm{o}} \mathbf{C}^{-1} \right]$	$C_p [J \cdot kg^{-1} \cdot {}^{o}C^{-1}]$	Calculated α [m ² ·s ⁻¹]
20	6.6	565	2.64
93	7.3	565	2.92
205	9.1	574	3.58
250	9.7	586	3.74
315	10.6	603	3.97
425	12.6	649	4.38
500	13.9	682	4.60

(d) Temperature measurement location

In the simulation, the location of the point where the thermal history is measured must be identical to the location of the thermocouples in the experiment in order to validate the graph theory approach. In the graph theory approach, the location of each node is identified by its Cartesian coordinates. A node closest to the sensor location, called the sensor node, was identified and its Cartesian coordinates were modified to match those of the sensor location prior to thermal simulation.

The sensor node was placed at a depth of 0.1 mm below the surface of the substrate to mimic the effect of the aluminum tape used to shield the thermocouples from forced convection losses. This node location is identified and shown in Figure 3. After thermal simulation, the thermal history of the sensor nodes were plotted against the experimental data reported by Heigel *et al* [19, 20].

(e) Measurement of error

Errors between the experimental thermal history and graph theory simulation were calculated by comparing the measured temperature to the graph theory predicted temperature at all instances in time. Two different methods of calculating errors were used in this work. Eqns. (20) and (21) show the Mean Absolute Percentage Error (MAPE) and Root Mean Square Error (RMSE), respectively. We note that the MAPE and RMSE error quantification metrics consider error for the entire thermal history over *n*-time steps, not simply the error at a single point.

$$MAPE = \frac{100\%}{n} \times \sum_{i=1}^{n} \left| \frac{T_i - \hat{T}_i}{T_i} \right|$$
 (20)

$$RMSE = \sqrt{\sum_{i=1}^{n} \frac{\left(T_i - \hat{T}_i\right)^2}{n}}$$
 (21)

In both equations, n is the number of instances in time that were compared over the duration of deposition (n = 1800 for Case A, n = 900 for Case B); i is the current instant in time, T_i is the measured temperature, and \hat{T}_i is the graph theory simulated temperature.

5 Results

The simulations were conducted in the MATLAB environment on a desktop personal computer with an AMD Ryzen Threadripper 3970X, @3.7 GHz CPU with 128 GB RAM onboard memory. Table 7 shows the corresponding errors and computation times for all simulations as a function of node density and meltpool temperature (T_0). The simulation is repeated three times for each scenario, and the uncertainty is quantified in terms of the standard deviation of the repetitions. Figure 12 presents the simulation results and thermal history for Case A and Case B with different node densities for the representative meltpool temperature $T_0 = 2200$ °C.

The computation time increases in a nonlinear manner as a function of the number of nodes, with diminishing improvement in precision in terms of MAPE and RMSE. For the simulation using one node per block (0.235 nodes/mm³) for Case A with $T_0 = 2200 \,^{\circ}\text{C}$, the MAPE was found to be approximately 10.5% and RMSE was 22 °C (viz., $1/10^{\text{th}}$ of the recorded peak temperature of 200 °C). The key result is that the computation time is ~4 minutes. For Case B, the error increases to 12% MAPE and 70 °C RMSE ($1/7^{\text{th}}$ of the peak temperature of 500 °C). With FE analysis, implemented by Heigel *et al.* [19, 20], the result is reported to take approximately 135 minutes using the inactive element method.

In Figure 12 the rise in temperature observed in the initial part of the build from the experimental data is consistently higher than the graph theory predictions. Further, in the graph theory predictions, the time-location of the maximum temperature occurs later than the experimental data. Several sources of error offer explanation as to the difference between the graph theory simulation and the measured values from the experiment. This error is produced in part by the gain factor (*g*) in Eq. (15) and (17), which influences the rate of heat diffusion in the graph theory approach.

Table 7. Summary table for Case A and Case B simulation. The number in the parentheses is the standard deviation over 3 replications.

				Graph Theory approach with different assumed meltpool temperatures T ₀						
	Build Time (min)	Node Density	Comput ation		900 °C		200 °C	$T_0 = 25$		FE model reported in Ref. [19, 20]
		(nodes/mm ³)	Time (min)	MAPE (%)	RMSE (°C)	MAPE (%)	RMSE (°C)	MAPE (%)	RMSE (°C)	MAPE (%)
		0.235	4	13.10 (1.36)	25.92 (1.62)	10.75 (1.95)	23.21 (2.84)	10.13 (4.48)	21.48 (6.88)	10.4
Case A	26		23	9.80 (0.61)	22.82 (0.99)	7.65 (1.28)	18.77 (2.05)	7.55 (2.34)	17.67 (3.75)	(computation time 136
			79	7.95 (1.62)	20.70 (1.65)	6.60 (1.10)	18.39 (1.41)	5.98 (2.59)	16.54 (2.89)	minutes)
		0.235	4	26.54 (2.57)	114.37 (11.48)	17.33 (1.61)	75.04 (5.25)	10.49 (2.82)	48.46 (11.63)	2.4
Case B	5	5	5 0.470 23 24.45 (1.89)	105.21 (8.23)	12.70 (0.54)	59.50 (2.42)	10.48 (0.90)	49.46 (3.58)	(computation time 136	
		0.706	79	22.56 (0.47)	97.95 (1.61)	12.48 (0.88)	57.80 (3.76)	12.38 (0.54)	53.28 (3.09)	minutes)

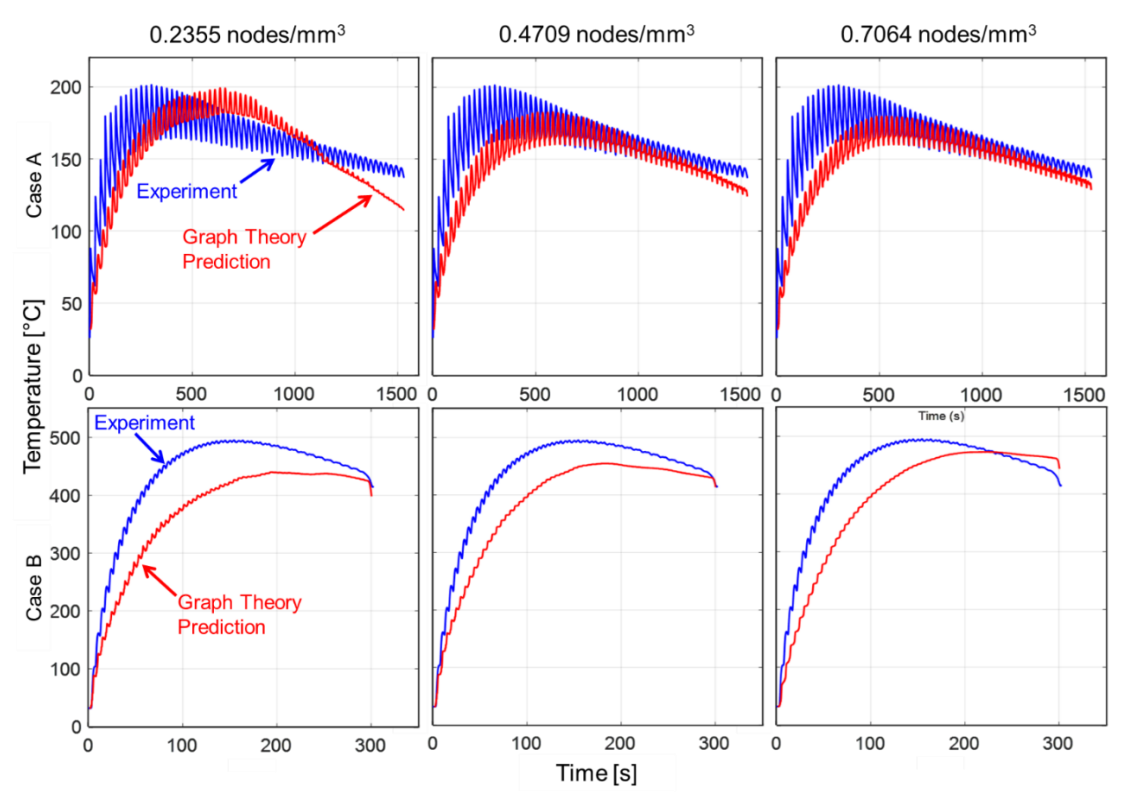


Figure 12. Graph theory simulation results for Case A and Case B for different node densities with $T_0 = 2200$ °C. The accuracy of prediction improves with increasing node density at the cost of computation time.

As discussed in Sec. 4.3.4, g and ε values were selected such that the error (MAPE) was minimized over the entire thermal history predicted by the graph theory approach for Case A when fitted to the corresponding experimental data. Since the rise time is a small fraction of the time domain, the gain factor (g), which is optimized over the entire time domain, somewhat favors the latter and longer duration of the temperature history at the expense of the initial rise. Another source of error is the free and forced convection assumption. The free (h_{free}) and forced convection coefficients (h_{forced}) are linked $(h_{forced} \approx 10 \times h_{free})$ and further connected to the heat loss at the clamp $(h_{clamp} \approx 20 \times h_{forced})$. Hence, an error in these heat transfer coefficients will propagate throughout the model.

Other sources of error include meltpool shape and temperature assumption used for the laser, stemming from Goldak's equation (Eq. (19), and the discretization of laser path as a block-by-block progression. These assumptions limit the accuracy of the model as a tradeoff to promote fast simulation, which was a key aim of the graph theory approach.

Lastly, the error between the experimental thermal history and graph theory simulation were found to be larger for Case B than for Case A. This is to be expected as the simulation parameters were calibrated based on experimental observations from Case A and directly applied to Case B. In converse, Heigel *et al.* calibrate their model parameters with Case B and apply them to Case A. As the deposition progresses, higher temperatures will be observed in the newly deposited layers. This is because as the height of the wall increases, its thin cross-section impedes the conduction of heat into the substrate.

The accumulation of heat in the upper layers is observed in the simulated spatiotemporal thermal history of the thin wall, exemplified in the images shown in Figure 13. Furthermore, in the graph theory simulations for Case A, the dwell time allows the heat to diffuse into the chamber

via convection and radiation, and into the substrate via conduction. In Case B, the accumulation of heat is severe in the top layers as the dwell time is not sufficient to dissipate the heat. Unlike FE analysis, where elements have a physical volume, in the graph theory approach the volume of the part is discretized as point nodes. In Figure 13, some regions of the part have no nodes, hence there are empty spaces in the temperature distribution. In our future work, we intend to interpolate the temperature in these areas where there are no nodes.

Next, we compared the FE-based predictions published by Heigel *et al.* [19, 20] with graph theory-predicted trends in Figure 14 for the representative case of 0.4709 nodes per mm³ and meltpool temperature $T_0 = 2200$ as it entails a reasonable tradeoff between computation time and accuracy. The graph theory approach for Case A predicts the experimental trends more precisely than the FE solution. Again, this is because the parameters for the graph theory approach are calibrated based on Case A trends. The performance of the FE approach is much improved for Case B compared to Case A, as the data from Case B was used by Heigel *et al.* to calibrate their FE model.

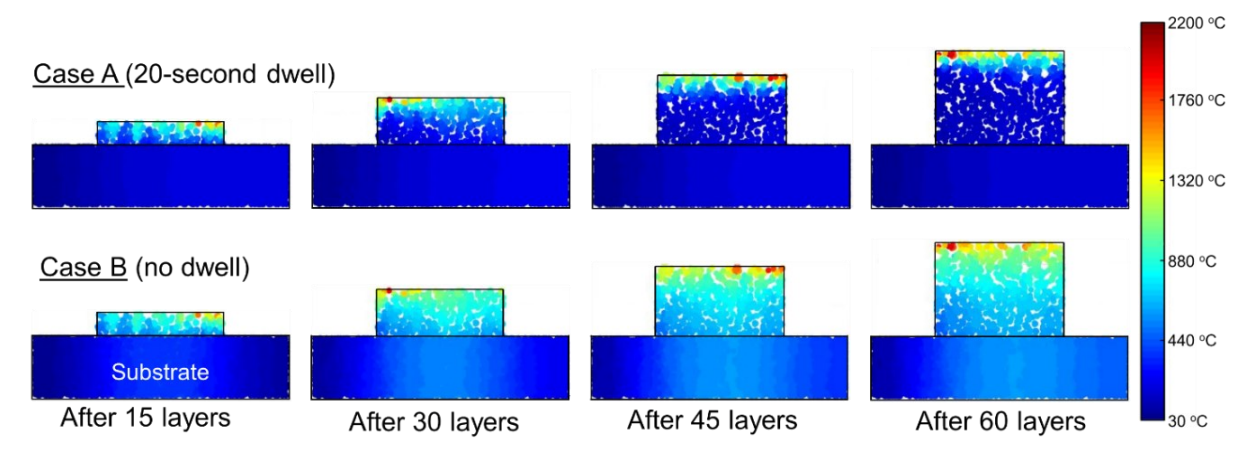


Figure 13: Snapshots of the graph theory-based simulation for Case A and Case B. The lack of dwell time in Case B leads to accumulation of heat in the top layers of the part. Because nodes take no physical space in this representation, some white spaces can be seen in this image.

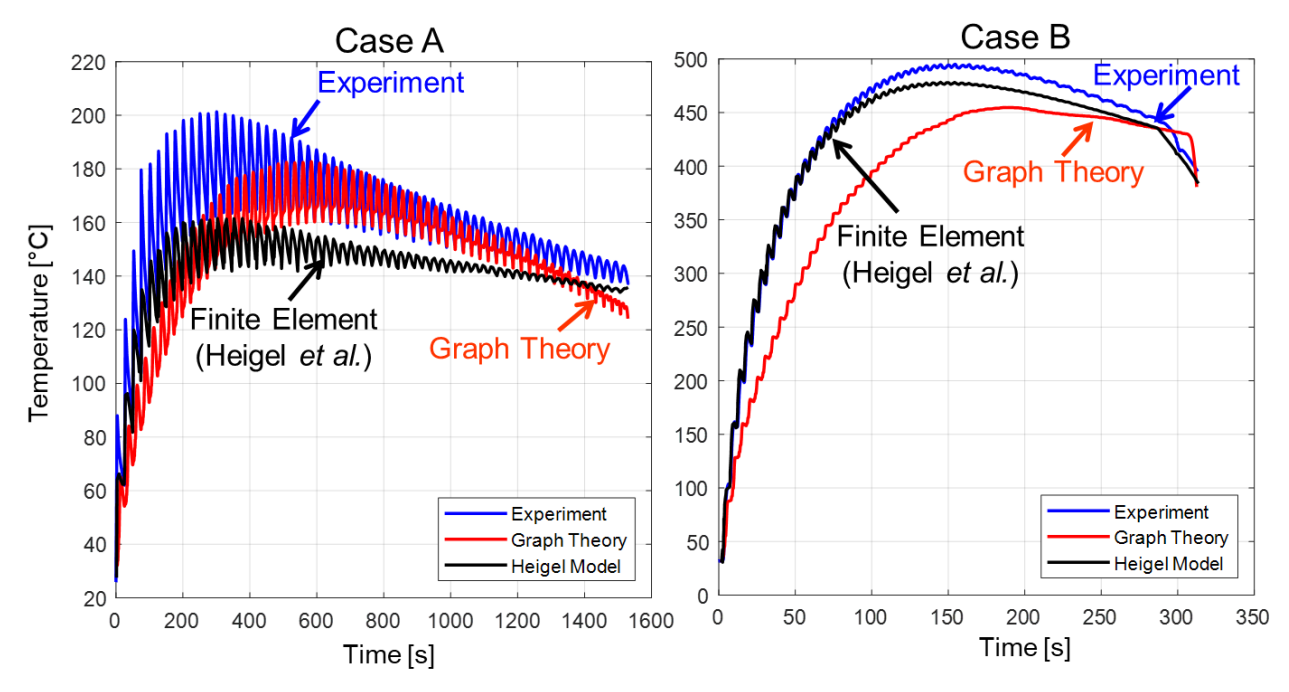


Figure 14: The comparison of the experimental data, with FE and graph theory predictions. The FE results are obtained from the work of Heigel *et al.* [19, 20].

6 Conclusions and Future Work

The objective of this work was to develop, apply, and validate a graph theory-based approach for thermal modeling in the directed energy deposition (DED) process. The graph theory method was validated with experimental temperature data for titanium alloy (Ti-6Al-4V) [19, 20]. Using the graph theory thermal modeling approach, practitioners can rapidly simulate the thermal history of DED components. This physical insight into the temperature distribution will be valuable for optimizing process conditions, such as laser power, part orientation and tool path, before the part is printed to avoid failures resulting from overheating. The approach can consequently reduce the need for an expensive build-and-test empirical optimization strategy, and thereby accelerate the time-to-market of DED parts.

The test parts are thin wall geometries with length ~37.2 mm, width ~3 mm, and vertical build height ~11 mm. The thin wall labeled Case A was deposited with a 20-second programmed dwell time between layers and the thin wall labeled Case B was deposited with no dwell time between layers. The build time for Case A is close to 26 minutes and 5 minutes for Case B. Several simulation scenarios were tested, including varying the resolution (number of nodes) and assumed melt pool temperature. Summarized below are results from a representative scenario that balances accuracy and computation time.

• For Case A, the graph theory approach predicts the temperature distribution with mean absolute percentage error (MAPE) less than 7% within 24 minutes of computation using desktop computing resources. The error is ~12% for Case B with the same computation time of 24 minutes. In comparison, the MAPE error reported by Heigel *et al.* using their FE-based model was ~10.5% (Case A) and 2.5% (Case B), with computation time 136 minutes.

 The simulation time can be reduced to as little as 4 minutes by sacrificing resolution of the simulation (reducing the number of nodes); The prediction error increases to ~ 10% for Case A and 17% for Case B.

The results substantiate the ability of the graph theory approach for fast *approximation* of the thermal history in DED. Several improvements to the graph theory model are currently being investigated to improve the model accuracy without sacrificing computational efficiency. These include modeling the laser as a heat source as opposed to a fixed temperature boundary condition, integrating the convection boundaries into the graph Laplacian matrix, allowing variable node density, and enabling increased accuracy in thermodynamically relevant regions near the laser source. In our future research, we will extend this work to the DED of complex part geometries using both in-situ measurement of local meltpool temperature and global part temperature. Finally, we will endeavor to relax the decoupled thermal-mechanical assumption endemic to almost all FE-based simulations of DED.

References

- [1] Cooke, S., Ahmadi, K., Willerth, S., and Herring, R., 2020, "Metal additive manufacturing: Technology, metallurgy and modelling," Journal of Manufacturing Processes, 57, pp. 978-1003. https://doi.org/10.1016/j.jmapro.2020.07.025
- [2] Smoqi, Z., Toddy, J., Halliday, H., Shield, J. E., and Rao, P., 2021, "Process-structure relationship in the directed energy deposition of cobalt-chromium alloy (Stellite 21) coatings," Materials & Design, 197, p. 109229. https://doi.org/10.1016/j.matdes.2020.109229
- [3] Saboori, A., Aversa, A., Marchese, G., Biamino, S., Lombardi, M., and Fino, P., 2019, "Application of directed energy deposition-based additive manufacturing in repair," Applied Sciences, 9(16), p. 3316.
- [4] Montazeri, M., Nassar, A. R., Stutzman, C. B., and Rao, P., 2019, "Heterogeneous sensorbased condition monitoring in directed energy deposition," Additive Manufacturing, 30, p. 100916. https://doi.org/10.1016/j.addma.2019.100916
- [5] Wolff, S., Lee, T., Faierson, E., Ehmann, K., and Cao, J., 2016, "Anisotropic properties of directed energy deposition (DED)-processed Ti–6Al–4V," Journal of Manufacturing Processes, 24, pp. 397-405. https://doi.org/10.1016/j.jmapro.2016.06.020
- [6] Stutzman, C. B., Nassar, A. R., and Reutzel, E. W., 2018, "Multi-sensor investigations of optical emissions and their relations to directed energy deposition processes and quality," Additive Manufacturing, 21, pp. 333-339. https://doi.org/10.1016/j.addma.2018.03.017

- [7] Sames, W. J., List, F., Pannala, S., Dehoff, R. R., and Babu, S. S., 2016, "The metallurgy and processing science of metal additive manufacturing," International Materials Reviews, 61(5), pp. 315-360.
- [8] Bandyopadhyay, A., and Traxel, K. D., 2018, "Invited Review Article: Metal-additive manufacturing—Modeling strategies for application-optimized designs," Additive Manufacturing [9] Foteinopoulos, P., Papacharalampopoulos, A., and Stavropoulos, P., 2018, "On thermal modeling of Additive Manufacturing processes," CIRP Journal of Manufacturing Science and Technology, 20, pp. 66-83. https://doi.org/10.1016/j.cirpj.2017.09.007
- [10] Wei, H. L., Mukherjee, T., Zhang, W., Zuback, J. S., Knapp, G. L., De, A., and DebRoy, T., 2021, "Mechanistic models for additive manufacturing of metallic components," Progress in Materials Science, 116, p. 100703. https://doi.org/10.1016/j.pmatsci.2020.100703
- [11] Denlinger, E. R., Gouge, M., and Michaleris, P., 2018, Thermo-Mechanical Modeling of Additive Manufacturing, Butterworth-Heinemann.
- [12] Yan, Z., Liu, W., Tang, Z., Liu, X., Zhang, N., Li, M., and Zhang, H., 2018, "Review on thermal analysis in laser-based additive manufacturing," Optics & Laser Technology, 106, pp. 427-441. https://doi.org/10.1016/j.optlastec.2018.04.034
- [13] Shassere, B., Nycz, A., Noakes, M. W., Masuo, C., and Sridharan, N., 2019, "Correlation of Microstructure and Mechanical Properties of Metal Big Area Additive Manufacturing," Applied Sciences, 9(4), p. 787.
- [14] Simunovic, S., Nycz, A., Noakes, M., Chin, C., and Oancea, V., "Metal big area additive manufacturing: Process modeling and validation," Proc. NAFEMS World Congress.
- [15] Simunovic, S., Nycz, A., Noakes, M. W., Chin, C., and Oancea, V., 2017, "Process Modeling and Validation for Metal Big Area Additive Manufacturing," Oak Ridge National Laboratory (ORNL), Oak Ridge, TN, https://www.osti.gov/servlets/purl/1399437.
- [16] Yavari, M. R., Cole, K. D., and Rao, P. K., 2019, "Thermal Modeling in Metal Additive Manufacturing using Graph Theory," ASME Transactions, Journal of Manufacturing Science and Engineering, 141(7), pp. 071007-071027. 10.1115/1.4043648
- [17] Cole, K. D., Yavari, M. R., and Rao, P. K., 2020, "Computational heat transfer with spectral graph theory: Quantitative verification," International Journal of Thermal Sciences, 153, p. 106383. https://doi.org/10.1016/j.ijthermalsci.2020.106383
- [18] Yavari, M. R., Williams, R. J., Cole, K. D., Hooper, P. A., and Rao, P. K., 2020, "Thermal Modeling in Metal Additive Manufacturing using Graph Theory: Experimental Validation with In-situ Infrared Thermography Data from Laser Powder Bed Fusion," ASME Transactions, Journal of Manufacturing Science and Engineering., 142(12), pp. 121005-121022.
- [19] Heigel, J. C., Michaleris, P., and Reutzel, E. W., 2015, "Thermo-mechanical model development and validation of directed energy deposition additive manufacturing of Ti–6Al–4V," Additive Manufacturing, 5, pp. 9-19. https://doi.org/10.1016/j.addma.2014.10.003
- [20] Heigel, J. C., 2015, "Thermo-Mechanical Model Development and Experimental Validation for Directed Energy Deposition Additive Manufacturing Processes," Doctor of Philosophy Dissertation, Pennsylvania State University, State College, PA.
- [21] Michaleris, P., 2014, "Modeling metal deposition in heat transfer analyses of additive manufacturing processes," Finite Elements in Analysis and Design, 86, pp. 51-60. https://doi.org/10.1016/j.finel.2014.04.003
- [22] Luo, Z., and Zhao, Y., 2018, "A survey of finite element analysis of temperature and thermal stress fields in powder bed fusion Additive Manufacturing," Additive Manufacturing, 21, pp. 318-332.

- [23] Tikare, V., Griffith, M., Schlienger, E., and Smugeresky, J., 1997, "Simulation of coarsening during laser engineered Net-Shaping," Sandia National Labs, Albuquerque, NM (United States).
- [24] Hofmeister, W., Wert, M., Smugeresky, J., Philliber, J. A., Griffith, M., and Ensz, M., 1999, "Investigation of Solidification in the Laser Engineered Net shaping (LENS) Process," Journal of Metals, 51(7)
- [25] Pinkerton, A. J., and Li, L., 2004, "The development of temperature fields and powder flow during laser direct metal deposition wall growth," Journal of Mechanical Engineering Science, 218(5), pp. 531-541. https://doi.org/10.1243/095440604323052319
- [26] Vasinonta, A., Beuth, J. L., and Griffith, M., 2007, "Process Maps for Predicting Residual Stress and Melt Pool Size in the Laser-Based Fabrication of Thin-Walled Structures," ASME Transactions, Journal of Manufacturing Science and Engineering, 129(1), pp. 101-109. https://doi.org/10.1115/1.2335852
- [27] Huang, Y., Khamesee, M. B., and Toyserkani, E., 2019, "A new physics-based model for laser directed energy deposition (powder-fed additive manufacturing): From single-track to multi-track and multi-layer," Optics & Laser Technology, 109, pp. 584-599. https://doi.org/10.1016/j.optlastec.2018.08.015
- [28] Wang, L., Felicelli, S. D., and Pratt, P., 2008, "Residual stresses in LENS-deposited AISI 410 stainless steel plates," Materials Science and Engineering A: Structural Materials, 496(1), pp. 234-241. https://doi.org/10.1016/j.msea.2008.05.044
- [29] Kelly, S. M., and Kampe, S. L., 2004, "Microstructural evolution in laser-deposited multilayer Ti-6Al-4V builds: Part II. Thermal modeling," Metallurgical and Materials Transactions A, 35(6), pp. 1869–1879. https://doi.org/10.1007/s11661-004-0095-7
- [30] Zheng, B., Zhou, Y., Smugeresky, J. E., Schoenung, J. M., and Lavernia, E. J., 2008, "Thermal Behavior and Microstructural Evolution during Laser Deposition with Laser-Engineered Net Shaping: Part I. Numerical Calculations," Metallurgical and Materials Transactions A, 39(9), pp. 2228–2236. https://doi.org/10.1007/s11661-008-9557-7
- [31] Jendrzejewski, R., Kreja, I., and Śliwińskia, G., 2004, "Temperature distribution in laser-clad multi-layers," Materials Science and Engineering A: Structural Materials, 379(1), pp. 313-320. https://doi.org/10.1016/j.msea.2004.02.053
- [32] Pratt, P., Felicelli, S. D., Wang, L., and Hubbard, C. R., 2008, "Residual Stress Measurement of Laser-Engineered Net Shaping AISI 410 Thin Plates Using Neutron Diffraction," Metallurgical and Materials Transactions A, 39(13), pp. 3155–3163. https://doi.org/10.1007/s11661-008-9660-9
- [33] He, X., Yu, G., and Mazumder, J., 2010, "Temperature and composition profile during double-track laser cladding of H13 tool steel," Journal of Physics D: Applied Physics, 43(1), p. 015502. https://doi.org/10.1088/0022-3727/43/1/015502
- [34] Lundbäck, A., and Lindgren, L.-E., 2011, "Modelling of metal deposition," Finite Elements in Analysis and Design, 47(10), pp. 1169-1177. https://doi.org/10.1016/j.finel.2011.05.005
- [35] Hoadley, A. F. A., Rappaz, M., and Zimmermann, M., 1991, "Heat-flow simulation of laser remelting with experimenting validation," Metallurgical and Materials Transactions B: Process Metallurgy and Materials Processing Science, 22(1), pp. 101-109. 10.1007/BF02672531
- [36] Dai, K., and Shaw, L., 2002, "Distortion minimization of laser-processed components through control of laser scanning patterns," Rapid Prototyping Journal, 8(5), pp. 270-276. 10.1108/13552540210451732
- [37] Gouge, M. F., Heigel, J. C., Michaleris, P., and Palmer, T. A., 2015, "Modeling forced convection in the thermal simulation of laser cladding processes," The International Journal of

- Advanced Manufacturing Technology, 79, pp. 307–320. https://doi.org/10.1007/s00170-015-6831-x
- [38] Foster, B., Beese, A. M., Keist, J. S., McHale, E., and Palmer, T., 2017, "Impact of interlayer dwell time on microstructure and mechanical properties of nickel and titanium alloys," Metallurgical and Materials Transactions A, 48(9), pp. 4411-4422.
- [39] Foster, B. K., 2015, "Characterization of Inconel® 625 and Ti-6Al-4V Laser Deposited Builds Manufactured with Varying Dwell Times," M.S. Thesis, Pennsylvania State University.
- [40] Yang, Q., Zhang, P., Cheng, L., Min, Z., Chyu, M., and To, A. C., 2016, "Finite element modeling and validation of thermomechanical behavior of Ti-6Al-4V in directed energy deposition additive manufacturing," Additive Manufacturing, 12, pp. 169-177. https://doi.org/10.1016/j.addma.2016.06.012
- [41] Lu, X., Lin, X., Chiumenti, M., Cervera, M., Hu, Y., Ji, X., Ma, L., Yang, H., and Huang, W., 2019, "Residual stress and distortion of rectangular and S-shaped Ti-6Al-4V parts by Directed Energy Deposition: Modelling and experimental calibration," Additive Manufacturing, 26, pp. 166-179. https://doi.org/10.1016/j.addma.2019.02.001
- [42] DebRoy, T., Wei, H., Zuback, J., Mukherjee, T., Elmer, J., Milewski, J., Beese, A. M., Wilson-Heid, A., De, A., and Zhang, W., 2018, "Additive manufacturing of metallic components—process, structure and properties," Progress in Materials Science, 92, pp. 112-224.
- [43] Mukherjee, T., Wei, H. L., De, A., and DebRoy, T., 2018, "Heat and fluid flow in additive manufacturing—Part I: Modeling of powder bed fusion," Computational Materials Science, 150, pp. 304-313. https://doi.org/10.1016/j.commatsci.2018.04.022
- [44] Gatsos, T., Elsayed, K. A., Zhai, Y., and Lados, D. A., 2020, "Review on Computational Modeling of Process–Microstructure–Property Relationships in Metal Additive Manufacturing," JOM, 72(1), pp. 403-419. 10.1007/s11837-019-03913-x
- [45] Schoinochoritis, B., Chantzis, D., and Salonitis, K., 2017, "Simulation of metallic powder bed additive manufacturing processes with the finite element method: A critical review," Proceedings of the Institution of Mechanical Engineers, Part B: Journal of Engineering Manufacture, 231(1), pp. 96-117.
- [46] Gibson, I., Rosen, D. W., and Stucker, B., 2014, Additive manufacturing technologies, Springer.
- [47] Williams, R. J., Davies, C. M., and Hooper, P. A., 2018, "A pragmatic part scale model for residual stress and distortion prediction in powder bed fusion," Additive Manufacturing, 22, pp. 416-425. https://doi.org/10.1016/j.addma.2018.05.038
- [48] King, W. E., Anderson, A. T., Ferencz, R. M., Hodge, N. E., Kamath, C., Khairallah, S. A., and Rubenchik, A. M., 2015, "Laser powder bed fusion additive manufacturing of metals; physics, computational, and materials challenges," Applied Physics Reviews, 2(4), p. 041304.
- [49] Goldak, J., Chakravarti, A., and Bibby, M., 1984, "A new finite element model for welding heat sources," Metallurgical Transactions B, 15(2), pp. 299-305. 10.1007/bf02667333
- [50] Goldak, J. A., and Akhlaghi, M., 2005, Computational Welding Mechanics, Springer, New York, NY, USA.
- [51] Gouge, M., and Michaleris, P., 2018, Thermo-Mechanical Modeling of Additive Manufacturing, Elsevier, Cambridge, MA.
- [52] Gouge, M., and Michaleris, P., 2017, Thermo-mechanical modeling of additive manufacturing, Butterworth-Heinemann.

- [53] Escolano, F., Hancock, E. R., and Lozano, M. A., 2012, "Heat diffusion: Thermodynamic depth complexity of networks," Physical Review E, 85(3), p. 036206. https://doi.org/10.1103/PhysRevE.85.036206
- [54] Xiao, B., Hancock, E. R., and Wilson, R. C., 2009, "Graph characteristics from the heat kernel trace," Pattern Recognition, 42(11), pp. 2589-2606. https://doi.org/10.1016/j.patcog.2008.12.029
- [55] Zhang, F., and Hancock, E. R., 2008, "Graph spectral image smoothing using the heat kernel," Pattern Recognition, 41(11), pp. 3328-3342. https://doi.org/10.1016/j.patcog.2008.05.007
- [56] Saito, N., 2013, "Tutorial: Laplacian Eigenfunctions Foundations and Applications," University of California, Davis, Graduate University for Advanced Studies, National Institute of Fusion Science, Japan.
- [57] Chung, F. R. K., 1997, Spectral graph theory, American Mathematical Society.
- [58] Yang, Y., Allen, M., London, T., and Oancea, V., 2019, "Residual Strain Predictions for a Powder Bed Fusion Inconel 625 Single Cantilever Part," Integrating Materials and Manufacturing Innovation, 8(3), pp. 294-304. 10.1007/s40192-019-00144-5
- [59] Mukherjee, T., Zhang, W., and DebRoy, T., 2017, "An improved prediction of residual stresses and distortion in additive manufacturing," Computational Materials Science, 126, pp. 360-372. https://doi.org/10.1016/j.commatsci.2016.10.003
- [60] Josupeit, S., Ordia, L., and Schmid, H.-J., 2016, "Modelling of temperatures and heat flow within laser sintered part cakes," Additive Manufacturing, 12, pp. 189-196. https://doi.org/10.1016/j.addma.2016.06.002
- [61] Hodge, N. E., Ferencz, R. M., and Vignes, R. M., 2016, "Experimental comparison of residual stresses for a thermomechanical model for the simulation of selective laser melting," Additive Manufacturing, 12, pp. 159-168. https://doi.org/10.1016/j.addma.2016.05.011
- [62] Afazov, S., Denmark, W. A. D., Lazaro Toralles, B., Holloway, A., and Yaghi, A., 2017, "Distortion prediction and compensation in selective laser melting," Additive Manufacturing, 17, pp. 15-22. https://doi.org/10.1016/j.addma.2017.07.005
- [63] Marques, B. M., Andrade, C. M., Neto, D. M., Oliveira, M. C., Alves, J. L., and Menezes, L. F., 2020, "Numerical Analysis of Residual Stresses in Parts Produced by Selective Laser Melting Process," Procedia Manufacturing, 47, pp. 1170-1177. https://doi.org/10.1016/j.promfg.2020.04.167
- [64] Desmaison, O., Pires, P.-A., Levesque, G., Peralta, A., Sundarraj, S., Makinde, A., Jagdale, V., and Megahed, M., "Influence of Computational Grid and Deposit Volume on Residual Stress and Distortion Prediction Accuracy for Additive Manufacturing Modeling," Proc. Proceedings of the 4th World Congress on Integrated Computational Materials Engineering (ICME 2017), pp. 365-374.
- [65] Peter, N., Pitts, Z., Thompson, S., and Saharan, A., 2020, "Benchmarking build simulation software for laser powder bed fusion of metals," Additive Manufacturing, 36, p. 101531. https://doi.org/10.1016/j.addma.2020.101531
- [66] Römer, G.-w., and Huis in 't Veld, A., "Matlab laser toolbox," Proc. International Congress on Applications of Lasers & Electro-Optics, Laser Institute of America, pp. 523-529.
- [67] Marshall, G., II, W. J. Y., Shamsaei, N., Craig, J., Wakeman, T., and Thompson, S. M., "Dual Thermographic Monitoring of Ti-6Al-4V Cylinders during Direct Laser Deposition," Proc. International Solid Freeform Fabrication Symposium, University of Texas at Austin, pp. 259-272. [68] Marshall, G. J., Thompson, S. M., and Shamsaei, N., 2016, "Data indicating temperature response of Ti-6Al-4V thin-walled structure during its additive manufacture via Laser Engineered Net Shaping," Data in Brief, 7, pp. 697-703. https://doi.org/10.1016/j.dib.2016.02.084

- [69] Marshall, G. J., Young, W. J., Thompson, S. M., Shamsaei, N., Daniewicz, S. R., and Shao, S., 2016, "Understanding the microstructure formation of Ti-6Al-4V during direct laser deposition via in-situ thermal monitoring," Jom, 68(3), pp. 778-790.
- [70] Khanzadeh, M., Chowdhury, S., Tschopp, M. A., Doude, H. R., Marufuzzaman, M., and Bian, L., 2018, "In-situ monitoring of melt pool images for porosity prediction in directed energy deposition processes," IISE Transactions, 51(5), pp. 437-455. https://doi.org/10.1080/24725854.2017.1417656
- [71] Lia, F., Park, J. Z., Keist, J. S., Joshia, S., and Martukanitz, R. P., 2018, "Thermal and microstructural analysis of laser-based directed energy deposition for Ti-6Al-4V and Inconel 625 deposits," Materials Science and Engineering A: Structural Materials, 717, pp. 1–10. https://doi.org/10.1016/j.msea.2018.01.060
- [72] Kriczky, D. A., Irwin, J., Reutzel, E. W., Michaleris, P., Nassar, A. R., and Craig, J., 2015, "3D spatial reconstruction of thermal characteristics in directed energydeposition through optical thermal imaging," Journal of Materials Processing Technology, 221, pp. 172-186. https://doi.org/10.1016/j.jmatprotec.2015.02.021
- [73] Yang, Q., Zhang, P., Cheng, L., Min, Z., Chyu, M., and To, A. C., 2016, "Finite element modeling and validation of thermomechanical behavior of Ti-6Al-4V in directed energy deposition additive manufacturing," Additive Manufacturing, 12(B), pp. 169–177. https://doi.org/10.1016/j.addma.2016.06.012
- [74] Wolff, S. J., Lin, S., Faierson, E. J., Liu, W. K., Wagner, G. J., and Cao, J., 2017, "A framework to link localized cooling and properties of directed energy deposition (DED)-processed Ti-6Al-4V," Acta Materialia, 132, pp. 106-117. https://doi.org/10.1016/j.actamat.2017.04.027